Computer Modeling in Engineering & Sciences
DOI:10.32604/cmes.2020.08204
Article

Solute Removal Analysis of a Large-Scale Fracture Plane Considering Different Flow Paths and Different Hydraulic Head Differences

Qian Yin[1,2], Xiaojing Li[3,*], Liyuan Yu[1], Ming He[1] and Richeng Liu[1,2]

[1]State Key Laboratory for Geomechanics & Deep Underground Engineering, China University of Mining and Technology, Xuzhou, 221116, China
[2]School of Engineering, Nagasaki University, Nagasaki, Japan
[3]School of Civil Engineering, Shandong Jianzhu University, Jinan, 116024, China
*Corresponding Author: Xiaojing Li. Email: li8021@163.com
Received: 06 August 2019; Accepted: 16 March 2020

Abstract: An experimental and numerical study was carried out to investigate the solute removal process through a large-scale fracture plane considering different flow paths and hydraulic head differences. The visualization techniques were utilized in the experiment to capture the removal process images, which were then transferred to binary images. The variations in dimensionless concentration, which is defined as saturation of solute phase, were analyzed. With increasing hydraulic head difference, the speed of solute removal increases and the dimensionless concentration decreases. The flow paths result in different solute distribution patterns and different mechanisms for solute removal such as advection and diffusion, thus the curves of dimensionless concentration versus time are different. The dimensionless concentration over time decreases from approximately 1, which is smaller than 1 due to the existence of bubbles, to approximately 0, which is larger than 0 because the folds of the background are dealt as "solute". A significant longer time is needed to achieve a certain fixed dimensionless concentration for a smaller hydraulic head difference. With the finite element software COMSOL multiphysics, the solute removal process, flow velocity fields, flow streamlines, as well as the hydraulic pressure fields were analyzed, which shows a good consistency with the experimental results. In practical engineering, when the solute pollutes the underground environment, the removal ability can be more significantly enforced by immediately applying a larger hydraulic head difference along a longer distance between the inlet and outlet boundaries.

Keywords: Solute removal; rock fracture; visualization; hydraulic head difference; flow path; numerical simulation

1 Introduction

When the nuclear materials from the Fukushima nuclear leakage accident and/or industrial waste water enter the deep underground, the groundwater is polluted and these solutes may transport in a wide range. To recovery the polluted groundwater, these solutes should be removed. Therefore, it is of special importance to understand the removal mechanism and removal process.

The previous studies commonly focused on the solute transport in fractured porous media, by considering advection and hydrodynamic dispersion, sorption reactions, and matrix diffusion [1–13]. Grisak et al. [14] described solute transport through a fractured media by combining fracture-dominated advective-dispersive transport and matrix-dominated diffusive transport. They found that the net effect of matrix that has a large diffusion coefficient can significantly reduce the effective solute velocity in the fracture. Hull et al. [15] performed laboratory and simulation studies of solute transport in fracture networks to analyze the transport of conservative solutes. They reported that the advection with the bulk fluid through the fracture networks plays a dominate role, which is referred to macrodispersion. Haldeman et al. [16] conducted a laboratory analysis of fluid flow and solute transport on a fracture porous tuff block that has a size of 20 × 20 × 50 cm. The results show that the significant channeling of fracture flow induces significant variations in breakthrough curves between experimental and simulation results. Kennedy et al. [17] developed a control volume model for calculating solute transport in a single fracture, which can estimate matrix diffusion in the direction parallel to fracture axis and consider the influence of boundary condition on two-dimensional matrix diffusion. Chen et al. [18] experimentally demonstrated contaminant removal from fractured rock through boiling. They reported that the chlorinated volatile compound is primarily removed by partitioning into vapor phase flow. Qian et al. [19] performed experiments to study flow and solute transport in a filled single fracture under non-Darcian flow conditions. Non-Fickian transport is found to dominate with early arrival and long tails, and mechanical filtration and intake of contaminant particles in dead or disconnected pore spaces can retard the transport. Sund et al. [20] extended the Spatial Markov model to upscale transport of a reacting solute across a diverse range of porous media flows, which can enforce the correlation between successive jumps and reproduce breakthrough curves that are measured from microscale simulations. Zhu et al. [21] proposed an analytical solutions of solute transport in a fracture-matrix system that considers different reaction rates for fracture and matrix. They concluded that the first-order reaction and matrix diffusion in the fracture rocks decrease the solute peak concentration and shorten penetration distance into the fracture. Liu et al. [22] derived a simple and robust solution for the problem of solute transport along a single fracture in a porous rock. This solution provided that the unchanged Peclet number with distance, which agrees with the observations in field experiments but cannot be predicted using the classical advection-dispersion equation. Delay et al. [23] provided a rigorous and detailed presentation of the partial differential equations ruling the continuous adjoint state associated with solute transport, and the method has been applied to four synthetic test cases targeting the estimation of hydraulic conductivity and effective porosity fields, using both piezometric heads and solute concentration data. Lucas et al. [24] conducted bench-scale solute injection experiments in a natural undisturbed basaltic fractured core to assess the performance of the equivalent apertures on conservative solute transport using an analytical solution of the one-dimensional advection-dispersion equation compared to observed breakthrough curves. Stanko et al. [25] demonstrated the feasibility of using proper orthogonal decomposition and discrete empirical interpolation method to reduce a solute transport model with nonlinear sorption and largely dispersive behavior. The results show that areas of high concentration are effectively identified with mean errors less than 2% of the full model. However, few of these studies investigated the solute removal process using visualization techniques and did not consider the effects of flow path and hydraulic head difference, which play an important role when clearing the polluted underground environment.

In the present study, a large-scale rough rock fracture was first manufactured and sealed, and then, red dye solute was injected into the model to represent the existing nuclear materials and/or industry waste water within the fractures. The pure water was consequently injected into the model to remove the solute and a high-resolution charged coupled device (CCD) camera was applied to capture the solute removal process. The captured color images were transferred to binary images using the software MATLAB by assigning a

threshold value, and the influences of flow paths and hydraulic head differences on the variations in dimensionless concentration were experimentally investigated. Then, using the finite element software COMSOL Multiphysics, the Navier-Stokes (NS) equations governing the flowing behavior though fractures were solved, and the flow velocity fields, flow streamline distributions, hydraulic pressure fields and solute removal processes of the fracture planes with respect to various inlet combinations and applied hydraulic head differences were numerically simulated and analyzed, as well as variations in the solute concentration.

2 Experiments and Procedures

2.1 Specimen Preparation

Two synthetic resinous plates are used to form the two walls of a fracture. Fluid/solute flows within the void spaces between the two walls. The length of the resinous plate is 65 cm and the width is 45 cm, as shown in Fig. 1a. Two large tanks are connected to the opposing sides of the model, providing water inflow and outflow, respectively. Four small tanks are added on the other two sides to supply water inflow to form different flow paths. For each tank, a valve is set to connect the tube connected to the water injection tank or the water storage tank. Next, two reinforced glass plates with a length of 55 cm and a width of 35 cm are put upon and below the model, after which four clips are adopted to clamp the two reinforced glass plates. This guarantees that during water injection, the two walls are not deformable and the aperture of the fracture can be fixed. When the solute removal is performed, pure water is injected into the model through inlets and collected at the outlet. The other valves connected to the inlets are closed.

2.2 Testing System and Procedure

Fig. 1b presents the flow testing system. An air compressor is used to supply a constant water head, which is connected to the inlet of the model. A high-resolution CCD camera is fixed upon the model to capture the solute removal process. This technique has been utilized for visualization analysis of fluid flow through single fractures or fracture networks in previous studies [26–30]. Therefore, here in this study, this kind of visualization technique is applied to analyze the solute removal process through single fracture planes with respect to various flow paths and various hydraulic head differences. The water that flows out of the model is collected in a storage tank, and the weight of the tank is weighted in time.

Before the tests, dye solute that has a concentration of 5 g/L is injected into the model to simulate the existed solute in the fracture. Then, the pure water is injected into the model to remove the solute, at the start of which, the time (t) is 0. When all the solute is removed, the constant water head is changed and another flow test continues. Three different water head differences (ΔH) of 14.8 cm, 57.3 cm, and 74.7 cm are adopted. After the solute removal images are captured using the CCD camera, they are imported into software MATLAB for image processing, in which the captured color images are transferred to binary images and the dimensionless concentration (or saturation of solute phase) is calculated and recorded. To remove the effect of clips on the image processing, an area that is smaller than the area of the reinforced glass plate such as 30 cm $\times$ 50 cm is chosen for observation as shown in Fig. 1b.

3 Experimental Results and Analysis

3.1 Solute Removal under Different Flow Paths for the Case of One Inlet

In the present study, "different flow paths" represent different combinations of inlet and outlet. Only the case of one inlet (inlet 1, or inlet 2, or inlet 3) and one outlet is considered in this section. The captured images and binary images over time for different inlets 1, 2 and 3 are exhibited in Figs. 2–4. After the dye solute is injected into the model, some bubbles exist as shown in Fig. 2a, which can represent the stress-induced damaged gauges within void spaces of a fracture in the nature. Fig. 2 shows the variations in the solute distribution over time by capturing experimental images and transferring them to the binary images for

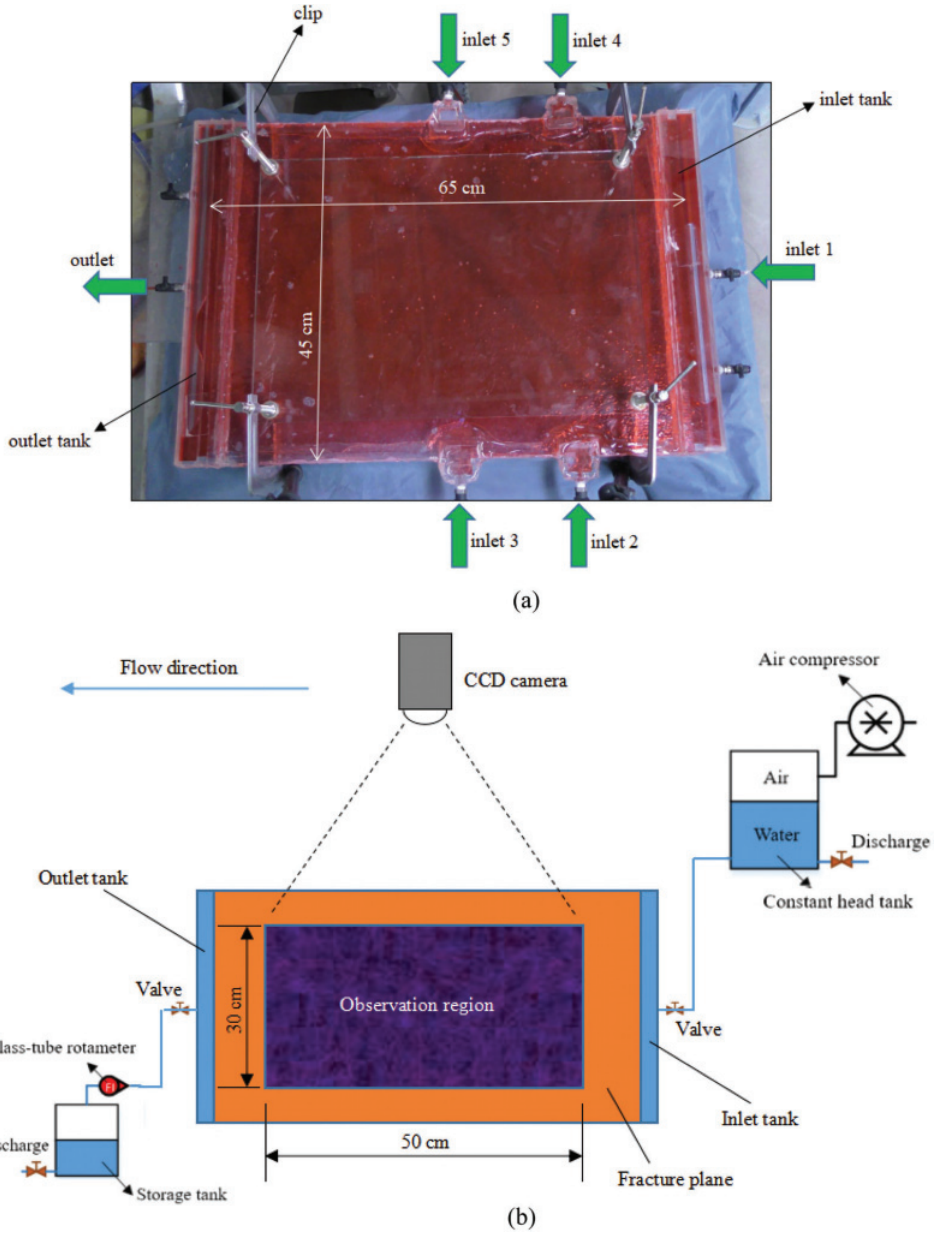

Figure 1: Experimental model and fluid flow testing system. (a) Experimental model. (b) Fluid flow testing system

the case of inlet 1 with $\Delta H = 74.7$ cm. The results show that with the increment of time, the solute is removed significantly. As a result, the dimensionless concentration defined as the area of solute to that of fracture plane over time decreases from approximately 1, which is smaller than 1 due to the existence of bubbles, to approximately 0, which is larger than 0 because the folds of the background are dealt as "solute". When $t < 400$ s, the solute removal is mainly dominated by advection; while for $t > 400$ s, there are some resident solute lines that are difficult to be removed in a short time. However, as the time increases, the color of the solute lines gradually bleaches, which indicates that the solute is removed due to diffusion. To quantitatively characterize the dimensionless concentration (or saturation of solute phase), the captured

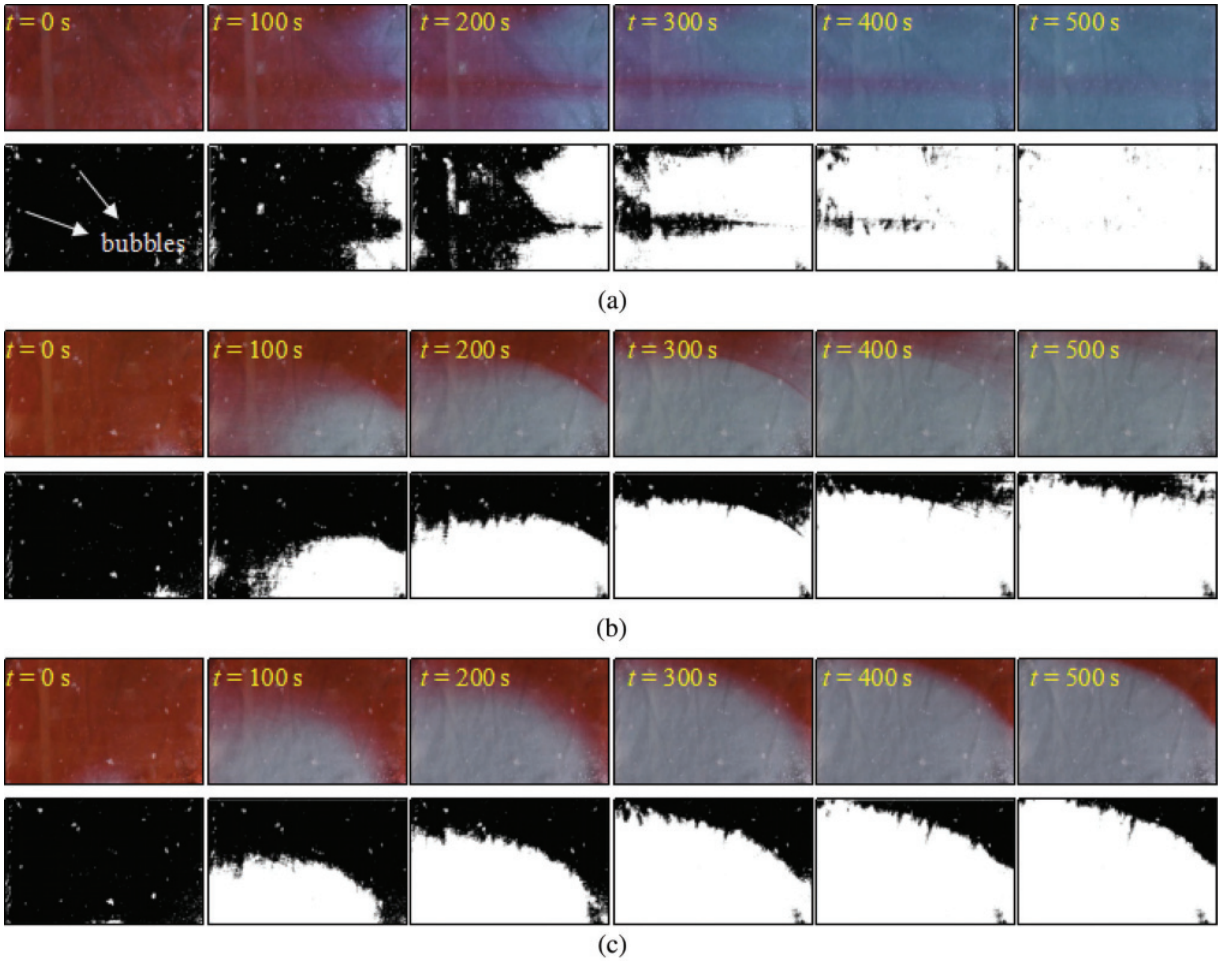

Figure 2: Captured images and binary images over time under a constant hydraulic head difference of 74.7 cm for (a) inlet 1, (b) inlet 2, and (c) inlet 3, respectively

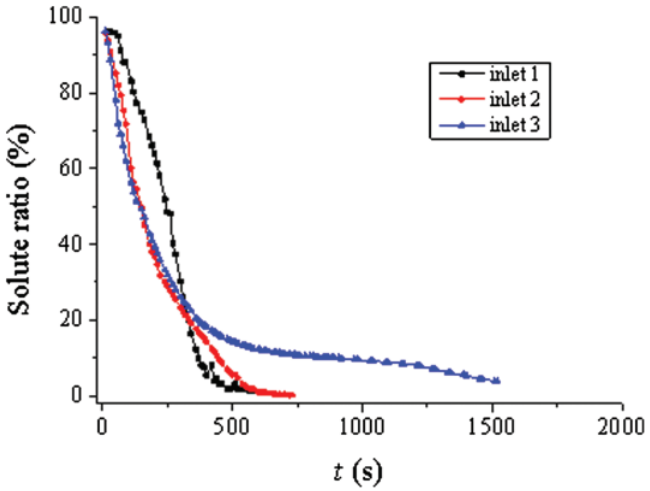

Figure 3: Variations in dimensionless concentration over time under a constant hydraulic head difference of 74.7 cm for single inlets

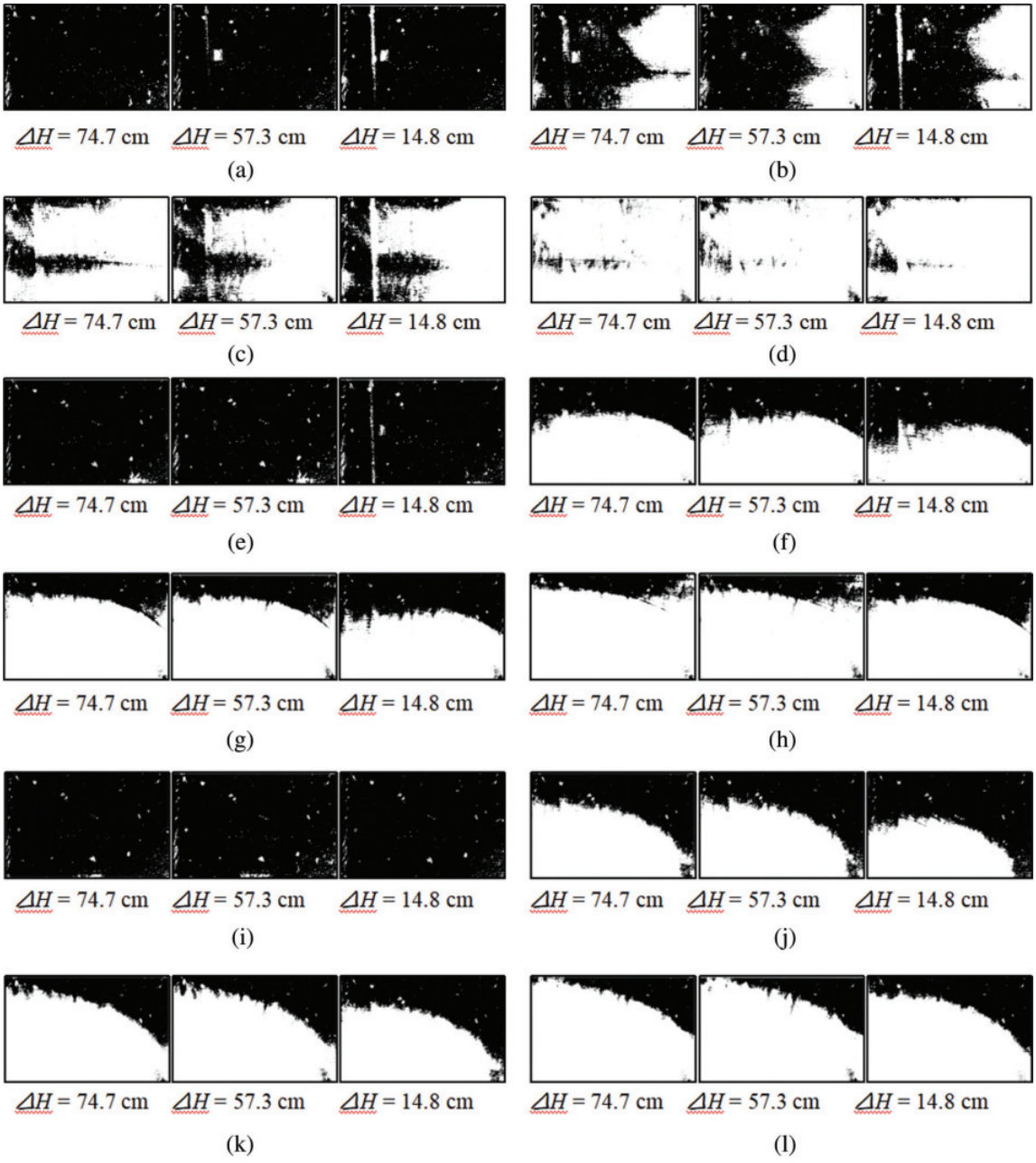

Figure 4: Binary images over time under different hydraulic head differences for the cases of inlet 1 (Figs. a–d), inlet 2 (Figs. e–h), and inlet 3 (Figs. i–l), respectively. (a) $t = 0$ s for the case of inlet 1, (b) $t = 200$ s for the case of inlet 1, (c) $t = 300$ s for the case of inlet 1, (d) $t = 400$ s for the case of inlet 1, (e) $t = 0$ s for the case of inlet 2, (f) $t = 200$ s for the case of inlet 2, (g) $t = 300$ s for the case of inlet 2, (h) $t = 400$ s for the case of inlet 2, (i) $t = 0$ s for the case of inlet 3, (j) $t = 200$ s for the case of inlet 3, (k) $t = 300$ s for the case of inlet 3, and (l) $t = 400$ s for the case of inlet 3

experimental images are processed using commercial software MATLAB. The experimental images are transferred to binary images by transferring the red dye solute to a black color and transferring the wathet background to a white color using a threshold value of 0.38 after a series of consistency characteristic

analysis of contours between the red dye solute and black binary images. The calculated binary images are depicted in Figs. 2(g)–2(l). Even though the binary images are not strictly consistent with the captured images due to reflection of light and dark color of the background, the binary images can generally represent the solute removal processes.

Figs. 3 and 4 depict the captured images and binary images over time for the cases of inlets 2 and 3, respectively. With the increase in time, the residual solute distributions for different flow paths (or inlets) are very different. For both cases, the solute cannot be completely removed even when t = 500 s, because some solutes near the upper boundary and/or the top right corner still exist and seem to be the "dead-ends" within fractures. The pure water cannot flow through this area, and solute is removed by diffusion, which takes a long time. Therefore, in practical engineering, to improve the removal ability, the distance between the inlet and outlet boundaries should be the longest, which can reduce the time that is needed for diffusion.

Fig. 5 shows the variations in dimensionless concentration over time for different flow paths (or inlets) under a constant ΔH of 74.7 cm. When the time is short (i.e., t < 300 s), the dimensionless concentration reduces significantly for the cases of inlets 2 and 3, followed by inlet 1, respectively. This is because the hydraulic gradient, defined as the ratio of hydraulic head difference to the length between inlet and outlet, is larger for the cases of inlets 2 and 3, comparing with that of inlet 1. The larger hydraulic gradient, the stronger removal ability, since at the beginning, the solute is removed

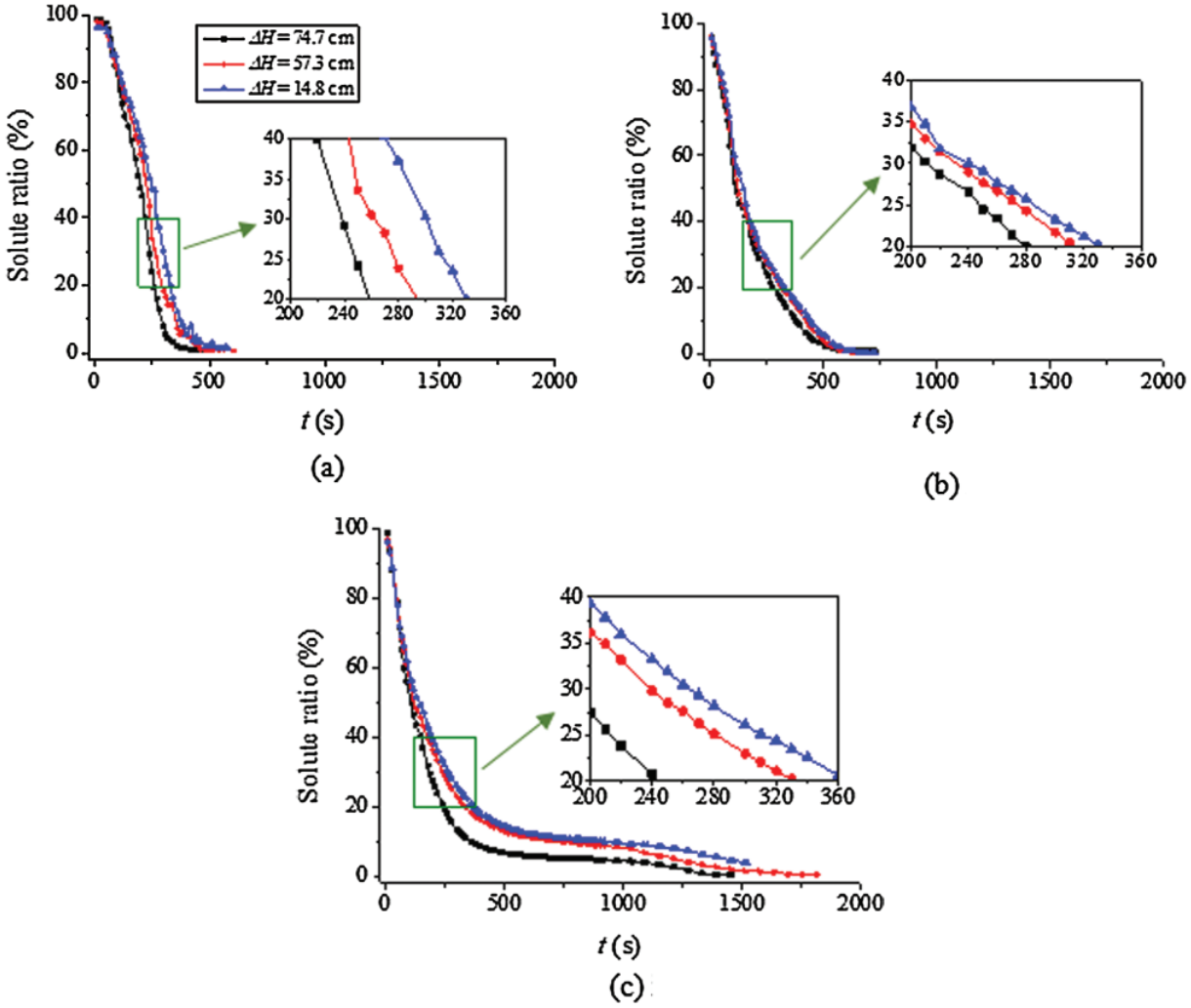

Figure 5: Variations in dimensionless concentration over time for single inlets under different hydraulic head differences. (a) inlet 1, (b) inlet 2, and (c) inlet 3

by advection. When the time is long (i.e., $t > 400$ s), the residual solute is small and it takes a short time to completely remove the solutes for the case of inlet 1. However, for the case of inlet 3, it takes a much longer time due to the existence of "dead-ends". The dimensionless concentration varies sufficiently small for t = 500–1000 s, because in this situation, although the concentration of the solute decreases, the area that the solute occupied does not change significantly. With continuously increasing t (i.e., $t > 1000$ s), the area that the solute occupied decreases because the solute in the "dead-ends" area is gradually removed. The shorter distance between the inlet and outlet boundaries, the longer time it takes to completely remove the solute.

3.2 Solute Removal under Different Hydraulic Head Differences for the Case of One Inlet

Figs. 6a–6d exhibit the variations in solute distributions under different ΔH varying from 14.8 cm to 74.7 cm for the case of inlet 1. For a certain solute removal time (i.e., t = 300 s), with the decrease in ΔH, the distributed area of solute increases, because the smaller ΔH, the weaker removal ability and the more solutes left over within the fractures. During this process, the bubbles within the fractures still exist and do not move along with fluid flow. For the case of inlet 1, the pure water is injected into the model along the right boundary; therefore, the velocity of fluid flow should theoretically be the same in the vertical direction. However, as shown in these images, there are some parts that fluid flows faster than other parts. This is induced by the rough fracture surface, which varies the aperture distribution along the vertical direction and then changes the fluid flow velocity. When the time is large (i.e., t = 500 s), the solute is removed, although there are still some black spots in the images. This is because the folds of the background are dealt as "solute".

Figs. 6e–6l present the variations in the solute distribution over time under different t for the cases of inlets 2 and 3, respectively. The results show the same trend as those presented in Figs. 6a–6d. With the decrease in ΔH, the dimensionless concentration increases. However, the pattern of solute distribution is different depending on the flow paths (inlets). Taking the case of inlet 3 as an example, the interface between solute and water shows a parabalo shape for $t > 300$ s, and this kind of solute distribution holds for a long time. This again illustrates that the water cannot flow through the "dead-ends", and the solute can only be removed by diffusion.

Fig. 7 shows the variations in dimensionless concentration (saturation of solute phase) versus time for different inlets and ΔH. The decrease rate of dimensionless concentration for the case of inlet 1 increases first and then decreases until the solute is completely removed. However, for the cases of inlets 2 and 3, the decrease rate of dimensionless concentration continuously decreases until the solute is completely removed. There exists a long stable stage in Fig. 7c, for example, t = 500–1000 s, because there are "dead-ends" in the models and the solute in this area cannot be removed by advection. They can only be removed by diffusion that takes a long time. After that ($t > 1000$ s), the solute is clearly removed by diffusion and the dimensionless concentration significantly decreases over time. Therefore, in practical engineering, it would take a long time if the solute transports into the "dead-ends" of a fracture. When the solute polluts the underground environment, the solute removal should be performed immediately, especially before the solute diffuses to the "dead-ends" of a fracture.

3.3 Solute Removal under Different Flow Paths for the Case of Two Inlets

In practical engineering, there may be multiple fractures connected to the polluted fracture, resulting in multiple inlets and/or outlets. In this section, two inlets and one outlet are considered. Five combinations are carried out to investigate the solute removal processes and variations in dimensionless concentration over time, including inlets 2 and 4, 3 and 5, 2 and 5, 1 and 2, and 1 and 3, respectively. The values of ΔH between the two inlets and outlet are both fixed as 74.7 cm. The captured images and binary images for the five cases are presented in Figs. 8 and 9. For the case of inlets 2 and 4 and the case of inlets 3 and 5,

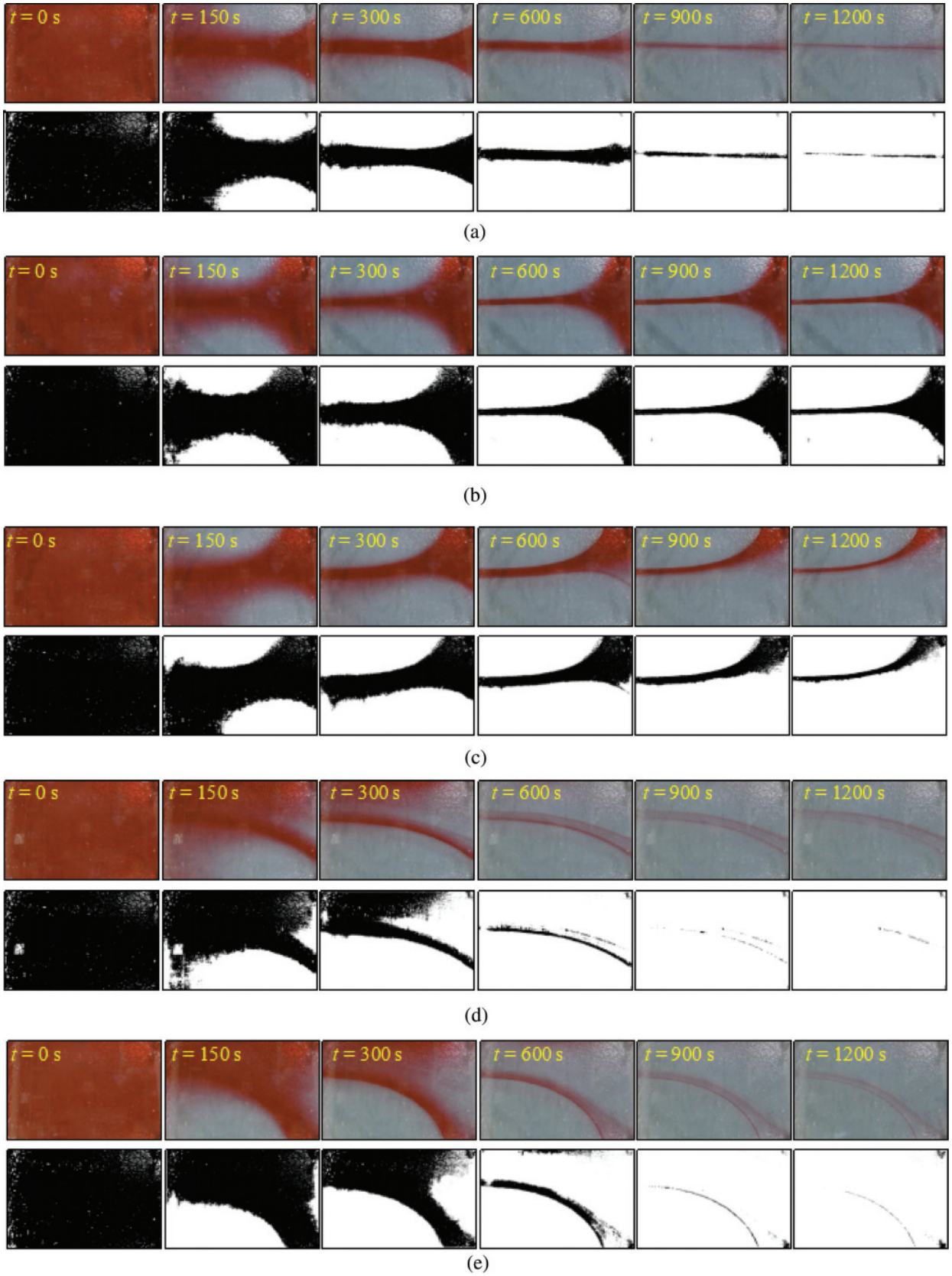

Figure 6: Captured images and binary images over time under a constant hydraulic head difference of 74.7 cm for (a) inlets 2 and 4, (b) inlets 3 and 5, (c) inlets 2 and 5, (d) inlets 1 and 2, and (e) inlets 1 and 3, respectively

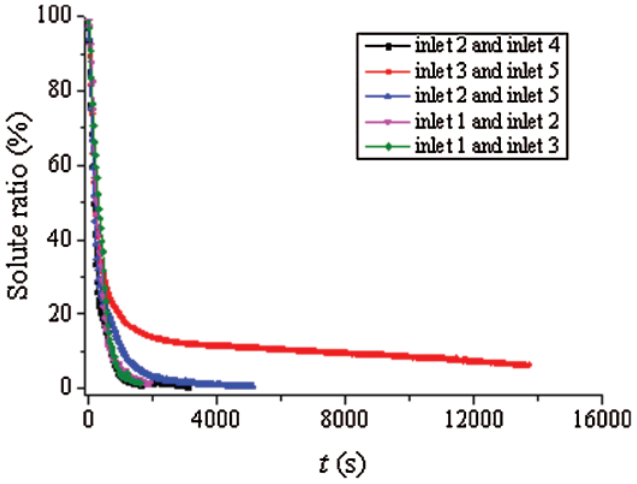

Figure 7: Variations in dimensionless concentration over time under a constant hydraulic head difference of 74.7 cm for two inlets

the two inlets for each case are axisymmetric and solute removal processes are also axisymmetric as shown in Figs. 8a–8b. For $t = 1200$ s, only a small part of solute is left in the middle of the model for the case of inlets 2 and 4, while for the case of inlets 3 and 5, a large amount of solute still exist in the right in the middle. This is because the inlets 2 and 4 are closer to the right boundary of the model, comparing with inlets 3 and 5, resulting in a smaller area for the "dead-ends". For the case of inlets 2 and 5 as depicted in Fig. 8c, although the values of ΔH for the two flow paths are the same, the hydraulic gradient between inlet 5 and outlet is larger than that between inlet 2 and outlet due to a shorter distance. As a result, the speed of solute removal at the start (i.e., $t < 300$ s) through inlet 5 is larger than that through inlet 2. Besides, the inlet 2 is closer to the right boundary and the solute in the bottom right corner can be more easily removed, comparing with that in the top right corner. For the case of inlets 1 and 2 and the case of inlets 1 and 3, the distributed patterns of solute over time are the same because inlet 1 is incorporated for both cases. The inlet 2 (or inlet 3) is closer to the outlet, resulting in a stronger removal ability than inlet 1. However, the solute in the top left corner that cannot easily be removed through fluid flow from inlet 2 (or inlet 3) will be removed through fluid flow from inlet 1, which takes a relatively long time.

Fig. 9 exhibits the variations in dimensionless concentration over time under a constant hydraulic head difference of 74.7 cm for the cases of two inlets. At first (i.e., $t < 500$ s), with the increment of time, the dimensionless concentration decreases significantly for all cases, showing the same trend. For $t > 1000$ s, the variations in dimensionless concentration are very different for different cases. For the case of inlets 3 and 5 that the two inlets are near the outlet and far from the right boundary, the dimensionless concentration decreases slightly and holds for a long time. This is because some "dead-ends" exist and the solute in the "dead-ends" is removed through diffusion, which is a time-consuming process. With the increase in the distance from the outlet (i.e., inlets 1 and 2, and 1 and 3), the time that is needed to completely remove the solute decreases. Therefore, to improve the removal ability of a polluted area, the pure water should be injected through the place that is the longest to the outlet.

3.4 Solute Removal under Different Hydraulic Head Differences for the Case of Two Inlets

In this section, the hydraulic head differences between the two inlets and outlet are the same, but vary from 14.8 cm to 74.7 cm. The binary images for solute distribution over time for five cases of inlets 2 and 4, 3 and 5, 2 and 5, 1 and 2, and 1 and 3, respectively, are presented in Figs. 10 and 11. With the increment of ΔH, the removal ability is increased, however, the solute distribution patterns are almost the same. Note that the

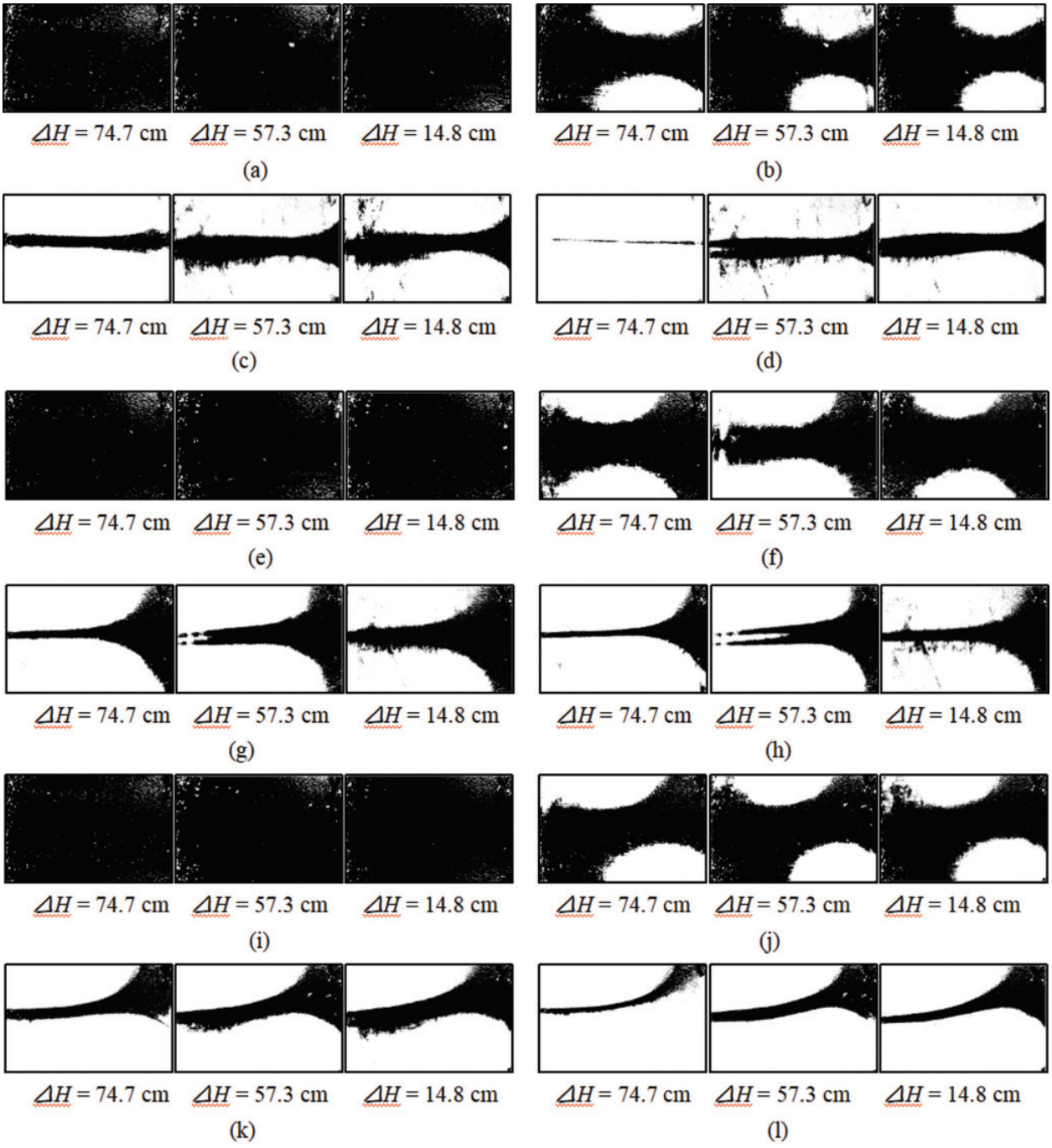

Figure 8: Binary images over time under different hydraulic head differences for the cases of inlets 2 and 4 (Figs. a–d), inlets 3 and 5 (Figs. e–h), and inlets 2 and 5 (Figs. i–l), respectively. (a) $t = 0$ s for the case of inlets 2 and 4, (b) $t = 150$ s for the case of inlets 2 and 4, (c) $t = 600$ s for the case of inlets 2 and 4, (d) $t = 1200$ s for the case of inlets 2 and 4, (e) $t = 0$ s for the case of inlets 3 and 5, (f) $t = 150$ s for the case of inlets 3 and 5, (g) $t = 600$ s for the case of inlets 3 and 5, (h) $t = 1200$ s for the case of inlets 3 and 5, (i) $t = 0$ s for the case of inlets 2 and 5, (j) $t = 150$ s for the case of inlets 2 and 5, (k) $t = 600$ s for the case of inlets 2 and 5, and (l) $t = 1200$ s for the case of inlets 2 and 5

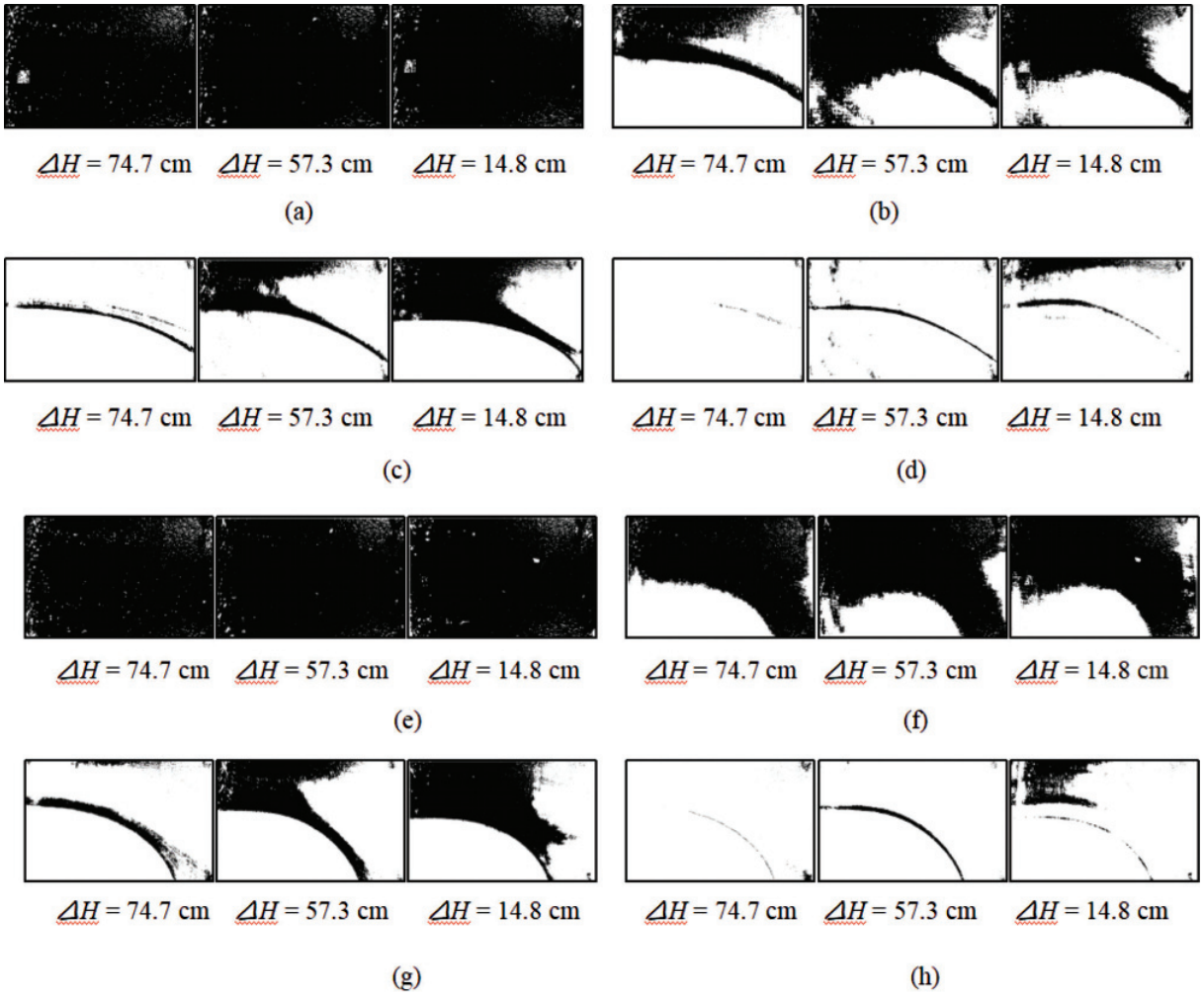

Figure 9: Binary images over time under different hydraulic head differences for the cases of inlets 1 and 2 (Figs. a–d), and inlets 1 and 3 (Figs. e–h), respectively. (a) $t = 0$ s for the case of inlets 1 and 2, (b) $t = 150$ s for the case of inlets 1 and 2, (c) $t = 600$ s for the case of inlets 1 and 2, (d) $t = 1200$ s for the case of inlets 1 and 2, (e) $t = 0$ s for the case of inlets 1 and 3, (f) $t = 150$ s for the case of inlets 1 and 3, (g) $t = 600$ s for the case of inlets 1 and 3, and (h) $t = 1200$ s for the case of inlets 1 and 3

removal ability is significantly enhanced for $\Delta H = 74.7$ cm when $t > 300$ s for the case of inlets 2 and 4, $t > 600$ s for the case of inlets 1 and 2 and the case of inlets 1 and 3, which are very different from other cases. The possible reason is that the increased ΔH can give rise to fluid flow enters the "dead-ends" for a smaller ΔH, resulting in the solute is removed through advection, rather than diffusion for the cases with a smaller ΔH.

Fig. 12 shows the variations in dimensionless concentration over time for two inlets under different ΔH. The results show that different combinations of inlets lead to different variations in dimensionless concentration. The case of inlets 3 and 5 takes a long time, while the case of inlets 1 and 2 and the case of inlets 1 and 3 take a relatively short time. The time needed to completely remove the solute is determined by the time needed to remove the solute in the "dead-ends". Increasing the value of ΔH from 14.8 to 74.7 cm will shorten the removal time to some extent. The influence of ΔH on dimensionless concentration is the most significant for the case of inlets 2 and 5. The selection of flow path is more important than increasing hydraulic head difference when removing solute within fractures.

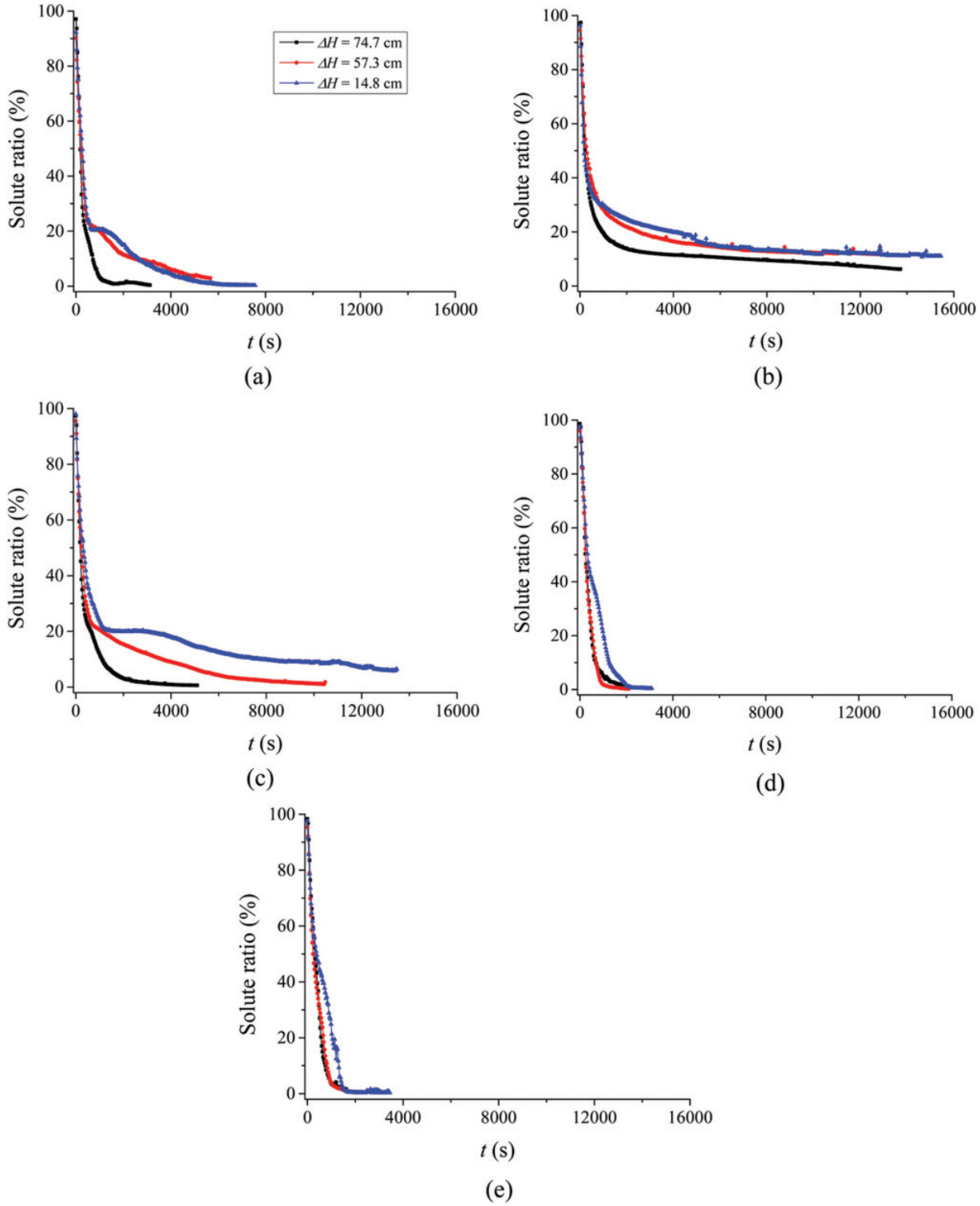

Figure 10: Variations in dimensionless concentration over time for two inlets under different hydraulic head differences. (a) inlets 2 and 4, (b) inlets 3 and 5, (c) inlets 2 and 5, (d) inlets 1 and 2, and (e) inlets 1 and 3

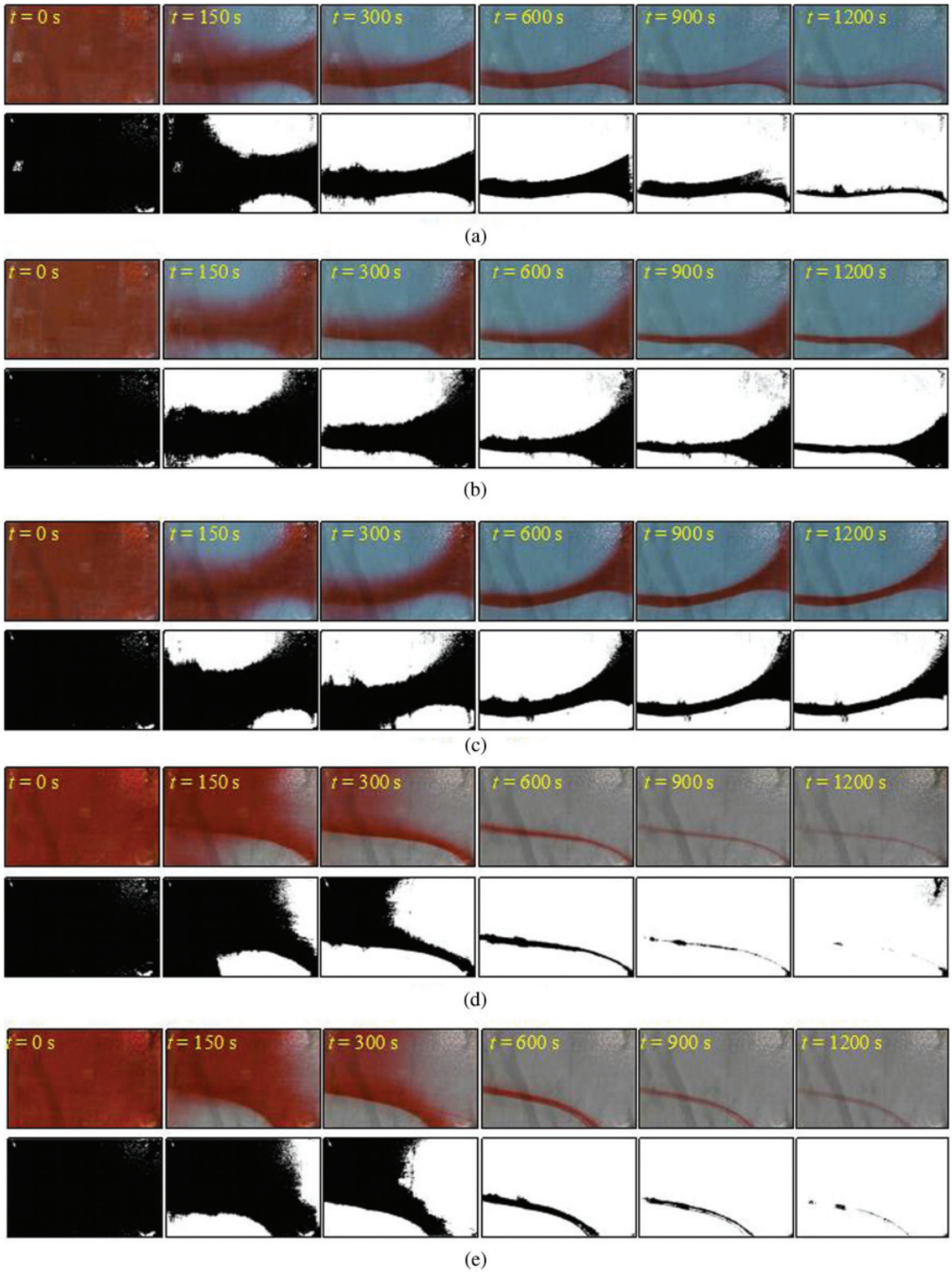

Figure 11: Captured images and binary images over time for the cases of (a) inlets 2 and 4, (b) inlets 3 and 5, (c) inlets 2 and 5, (d) inlets 1 and 2, and (e) inlets 1 and 3, with two hydraulic head differences of 14.8 cm and 74.7 cm, respectively

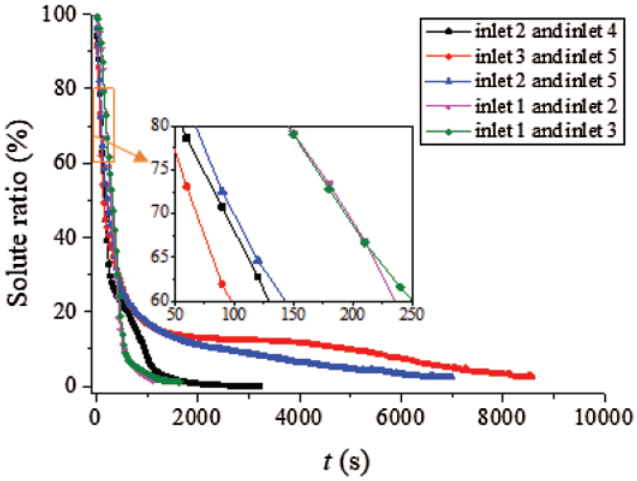

Figure 12: Variations in dimensionless concentration over time for two inlets with two hydraulic head differences of 14.8 cm and 74.7 cm, respectively

3.5 Solute Removal under Different Flow Paths for Two Inlets with Two Hydraulic Head Differences

In the nature, the fractures connected to the polluted fracture may have different hydraulic heads, which results in that the hydraulic head differences between the two inlets and outlet may be different. In this section, two inlets are considered and values of ΔH for the two flow paths are 14.8 cm and 74.7 cm, respectively. The five cases as illustrated in Sections 3.3 and 3.4 are designed. All the cases include inlets 2 or 3. Therefore, the value of ΔH for the inlets 2 or 3 is 14.8 cm and that for the other inlet is 74.7 cm. The solute distributions over time are exhibited in Fig. 13. The results show that the solute distribution moves downwards, with respect to those in Figs. 10 and 11, because the upper inlet has the larger value of ΔH and thereafter the strong removal ability of solute. With increasing t from 300 s to 600, the solute distribution varies slightly for the cases of inlets 2 and 4, 3 and 5, and 2 and 5, whereas changes significantly for the cases of inlets 1 and 2, and inlets 1 and 3, in which inlet 1 is incorporated. When inlet 1 is included (i.e., the cases of inlets 1 and 2, and 1 and 3), the role of inlet 1 played increases as the time increases. Taking t = 150–300 s in Fig. 13e as an example, the area of solute removed through

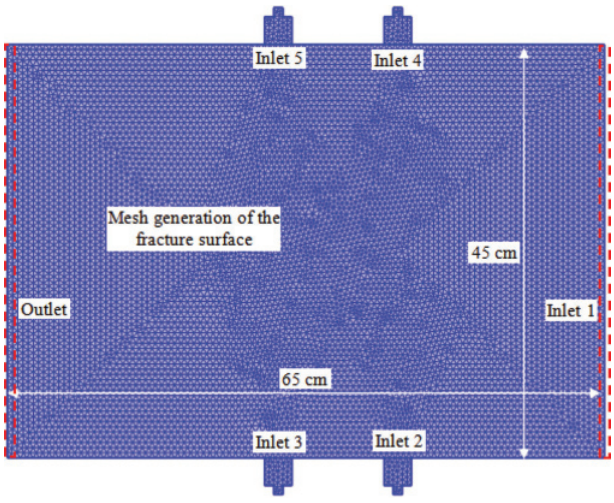

Figure 13: Numerical model setup and mesh generation

fluid from inlet 3 at $t = 150$ s is larger than that from inlet 1, since the inlet 3 is closer to the outlet, while the area of solute removed through fluid from inlet 3 at $t = 300$ s is smaller than that from inlet 1. This indicates that at the start of solute removal, the inlet near the outlet plays a dominate role, whereas with increasing the time, the inlet far from the outlet plays a dominate role due to its ability to remove the solute in the "dead-ends".

The variations in dimensionless concentration over time for two hydraulic head differences of 14.8 cm and 74.7 cm are exhibited in Fig. 14. With the increment of time, dimensionless concentration decreases first significantly and then gently. The decreasing rate decreases for all cases. In the rapid decreasing stage, i.e., $t =$ 50–250 s, the removal ability is stronger for the case with inlets that are closer to the outlet (i.e., the case of inlets 3 and 5). In the slow decreasing stage, i.e., $t > 500$ s, the solute removal is dominated by the diffusion. In such a case, the removal ability is stronger for the case with inlets that are longer to the outlet (i.e., the case of inlets 1 and 2) and is weaker for the case with inlets that are closer to the outlet (i.e., the case of inlets 3 and 5). Therefore, to improve the effectivity of solute removal, pure water should be injected into the polluted area in the place near the outlet at the beginning and injected into the polluted area in the place far from the outlet at the residual stage of solute removal.

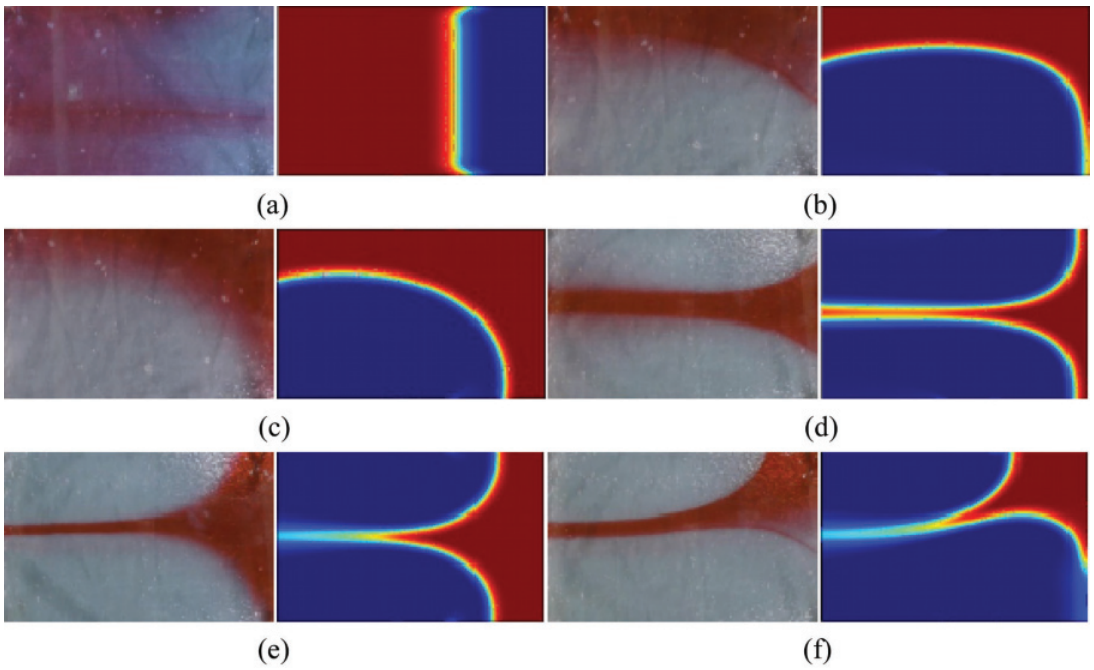

Figure 14: Comparison between experimental and numerically simulated solute removal characteristics of the fracture surface at $\Delta H = 74.7$ cm. (a) inlet 1, $t = 200$ s, (b) inlet 2, $t = 200$ s, (c) inlet 3, $t = 200$ s, (d) inlets 2 and 4, $t = 300$ s, (e) inlets 3 and 5, $t = 600$ s, (f) inlets 2 and 5, $t = 600$ s

4 Numerical Simulation

4.1 Governing Equations and Numerical Methods

Fluid flowing through single fractures can be generally governed using the Navier-Stokes (NS) equations and mass conservation equations, which can be written as follows for a steady-state and incompressible Newtonian fluid in an isothermal condition [7,29,31–32].

$$\rho(\mathbf{u} \cdot \nabla)\mathbf{u} = -\nabla P + \mu\nabla^2\mathbf{u} \tag{1}$$

$$\nabla \cdot \mathbf{u} = 0 \tag{2}$$

where $\mathbf{u}$ (m/s), P (Pa), ρ (kg/m^3) and μ (Pa·s), respectively, denote the flow velocity vector, hydraulic pressure, flow density and dynamic viscosity.

The Navier-Stokes equations are composed of a set of coupled nonlinear partial derivatives of varying orders characterizing the flow velocity and pressure fields. Here in this study, the generic finite element software COMSOL Multiphysics was employed to solve these equations, due to its own advantages of various physical modules, direct coupling analysis, independent parameter control, powerful mesh generation capability, strong computing power and rich post-processing functions [33–34].

4.2 Model Setup and Boundary Conditions

To carry out the numerical analysis, a two-dimensional rectangle model with the size of 45 × 65 cm, which is consistent with the experimental model, was set up, as shown in Fig. 13. Meshes with a total of 16686 triangular elements were generated for discretization of the model, with a high density and quality, to guarantee sufficient accuracy and good iteration convergence in the simulation.

The model was equipped with five various inlets, located at the right model boundary (inlet 1), middle (inlets 3 and 5) and quarter (inlets 2 and 4) positions of both the upper and lower model boundaries respectively. The hydraulic sources of these inlets could be individually switched on or off to control various flowing paths through the fracture surfaces, with the outlet located at the left model boundary. In order to simulate the fluid flowing process in the experiment, three different hydraulic heads ΔH of 14.8, 57.3 and 74.7 cm were respectively fixed at the water inlets. The hydraulic head at the water outlet of the fracture was zero for all models, and other model boundaries were set to be impermeable. Eight various flowing directions were respectively chosen by varying the inlet combinations (inlet 1, inlet 2, inlet 3, inlets 1 and 2, inlets 1 and 3, inlets 2 and 4, inlets 3 and 5, and inlets 2 and 5). During the simulation, the two-phase peristaltic flow module was chosen, and the water was assumed to be laminar, isothermal, viscous and incompressible Newtonian fluid, with the input ρ and μ values of 998.2 kg/m^3 and 1.307 × 10^{-3} Pa·s, respectively.

4.3 Numerical Model Validation

Before the numerical calculation, the micro parameters for the model were first calibrated by using the "trial and error" method. Through a large number of trial calculations, the fracture channel thickness b of 1 mm, the mobility tuning parameter χ of 1 m·s/kg, the contact angle θ_w of pi/2, the surface tension coefficient σ of 7 × 10^{-2} N/m, and the solute concentration λ of 5 g/L, were finally confirmed.

Fig. 14 shows a typical comparison between the experimental and numerically simulated solute removal characteristics of the fracture surface at ΔH = 74.7 cm. It can be seen that, at the same time, the simulated solute distributions generally exhibit a good agreement with the experimental results. For the case of inlet 1, in the experiment, the solute shows a stripe shape along the flowing direction, spacing by transparent pure water, while in the simulation, the solute is generally driven along the whole fracture width. The above phenomenon is might due to a certain unbalanced water pressure in the inlet at the beginning of the experiment. For the cases of inlets 2 and 3, the flowing behavior is consistent in the experiment and simulation, and the red solute is mainly concentrated in the upper region of the fracture surface at t = 200 s. The boundaries between the solute and pure water present a parabolic shape. For the cases of inlets 2 and 4 and inlets 3 and 5, both the experimental and numerical boundaries show trumpet shapes as a result of symmetrical applied hydraulic head differences at the upper/lower inlets of the fracture, rather than concentrated at the upper right corner for the case of inlets 2 and 5 in Fig. 14f. From the above analysis, we can find that the numerical simulation could accurately reflect the solute transport process through the fracture surfaces in the experiment.

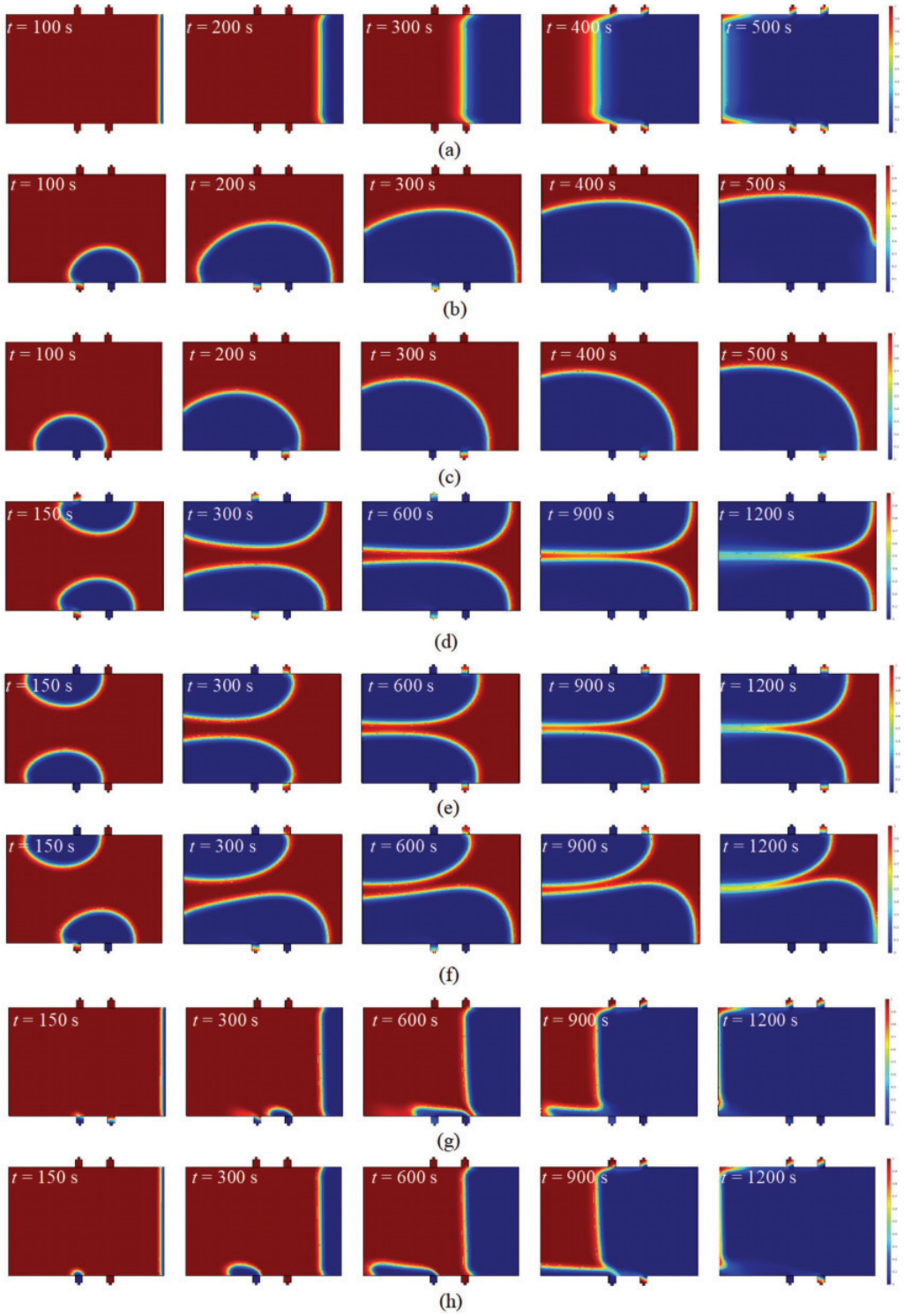

Figure 15: Numerical solute removal process of fractures with various inlets. (a) inlet 1, (b) inlet 2, (c) inlet 3, (d) inlets 2 and 4, (e) inlets 3 and 5, (f) inlets 2 and 5, (g) inlets 1 and 2, (h) inlets 1 and 3

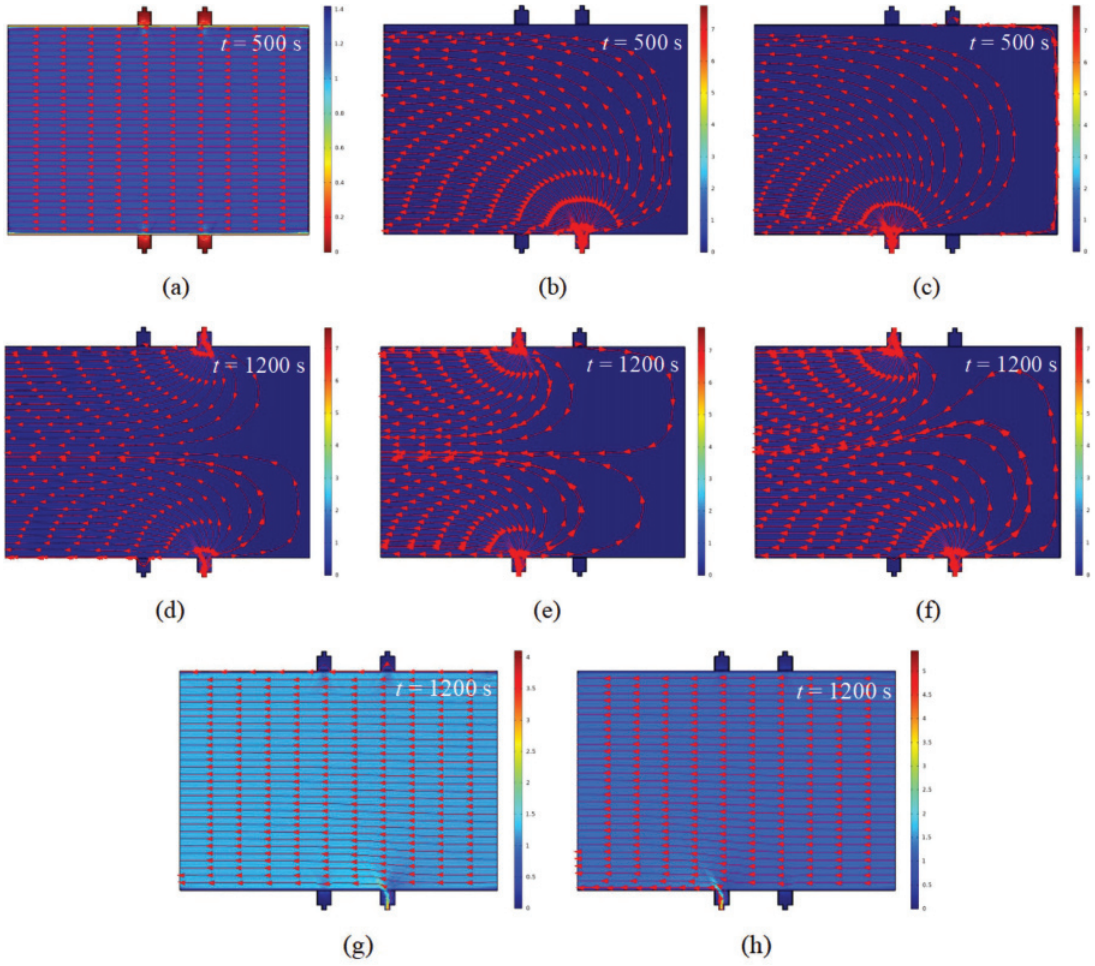

Figure 16: Flow velocity fields and flow streamlines for various inlets at ΔH = 14.8 cm. (a) inlet 1, (b) inlet 2, (c) inlet 3, (d) inlets 2 and 4, (e) inlets 3 and 5, (f) inlets 2 and 5, (g) inlets 1 and 2, and (h) inlets 1 and 3

4.4 Simulation Results and Discussion

The solute removal processes through the fracture surfaces with various inlets at ΔH = 14.8 cm are presented in Fig. 15. Similar to the experimental findings, as t increases, the solute is also driven remarkably, resulting in a decrease in the dimensionless concentration. Notably, the decrease rate of the solute area diminishes with t. Taking the case of inlet 2 as an example, for t = 100 and 200 s, the interface between the solute and pure water shows a semicircle shape. Then, for t = 300, 400 and 500 s, the semicircle generally transforms to a parabolic shape, and the parabola tends to be stable. From Figs. 15d–15f, due to opposite inlet water flowing directions from the upper and lower fracture boundaries, flowing channels of the residual solute gradually narrow, with gradually weakened solute concentrations. As t increases from 600 to 1200 s, the red solute gradually turns light blue. For the cases of inlets 1 and 2 and inlets 1 and 3, fluid flowing from the two inlets gradually mixes together, and at t = 1200 s, the solute is generally completely driven from the fracture planes.

Fig. 16 presents the flow velocity fields and flow streamlines on the fracture planes for various inlets at ΔH = 14.8 cm. Significant differences of the flow streamlines for various inlet combinations can be observed. For inlet 1, the solute removes along the horizontal direction from the inlet to outlet, with parallel flow streamlines. For inlets 2 and 3, the flow streamlines first diverge from the inlet, and then change the

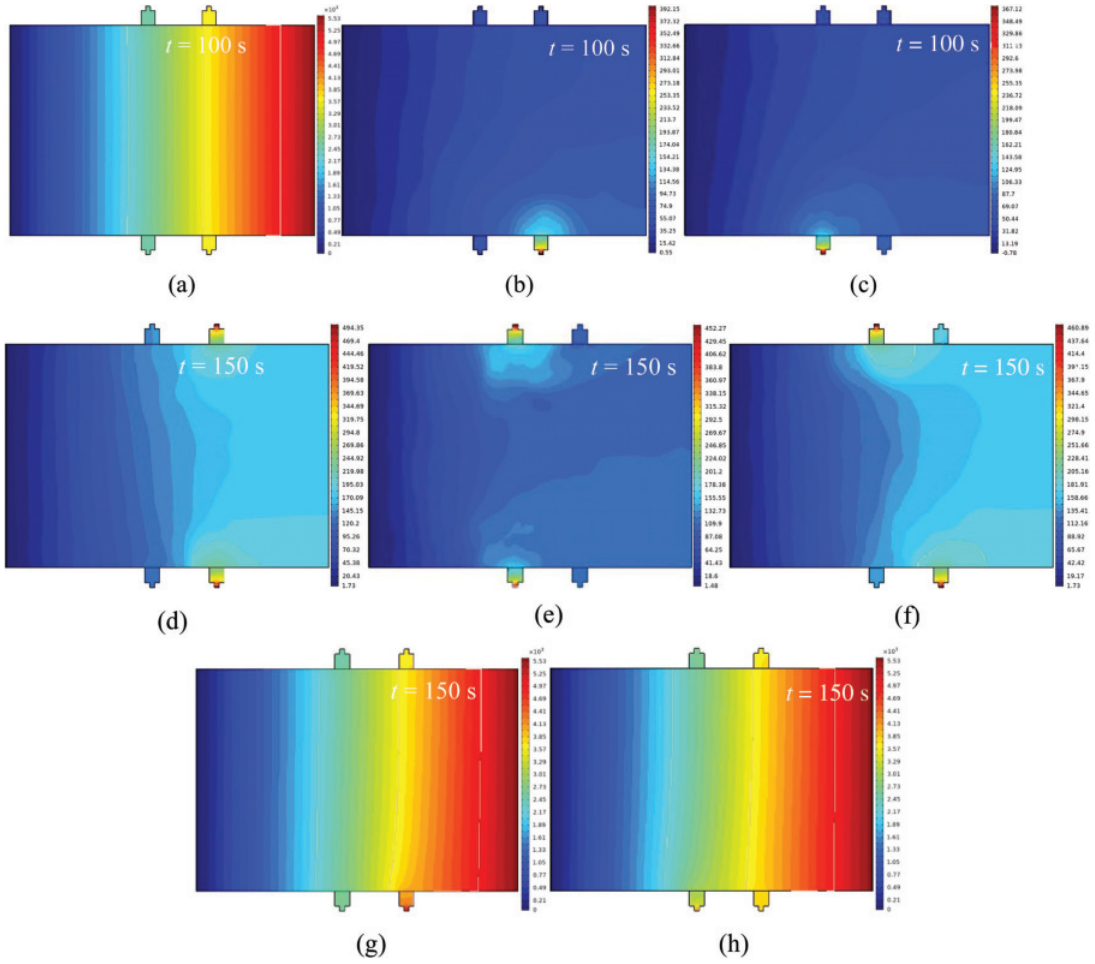

Figure 17: Hydraulic pressure fields for various inlets at $\Delta H = 57.3$ cm. (a) inlet 1, (b) inlet 2, (c) inlet 3, (d) inlets 2 and 4, (e) inlets 3 and 5, (f) inlets 2 and 5, (g) inlets 1 and 2, and (h) inlets 1 and 3

flowing directions to the zero water pressure boundary. For inlets 2 and 4, inlets 3 and 4, and inlets 2 and 5, flow streamlines from the two inlets gradually develop and coalesce, finally flowing along the horizontal direction to the outlet. Notably, eddy flow and turbuient flow can be observed near the inlets due to changes in the flow directions. However, for inlets 1 and 2 and inlets 1 and 3, the flow streamlines generally distribute along the horizontal direction, which is similar to that of inlet 1 in Fig. 16a. It is due to the fact that the flow area of inlet 1, which is much larger than that of inlets 2 or 3, plays a dominant role in the solute removal process of the fracture surfaces. The various flow streamlines will certainly result in various hydraulic pressure fields, as shown in Fig. 17 (ΔH = 57.3 cm). For inlet 1, the hydraulic pressure P presents a uniform weakening trend along the flowing path, indicating an equal P value along a given fracture width. For inlets 2 and 3, P first exhibits a layered attenuation from the inlet, and then gradually reduces to a generally stable P field near the outlet. Figs. 17d–17f indicate that hydraulic pressure fields on the fracture planes are relatively complex due to the opposite inlets. The P fields for the cases of inlets 1 and 2 and inlets 1 and 3 are generally similar to that of inlet 1 due to its dominant flow capacity.

The effects of hydraulic head ΔH and t on the flow velocity fields, flow streamlines and solute removal processes for the fracture surfaces with various inlets are presented in Figs. 18–22. It can be seen that, an increase in ΔH has almost no influence on the distribution patterns of the flow velocity fields or hydraulic

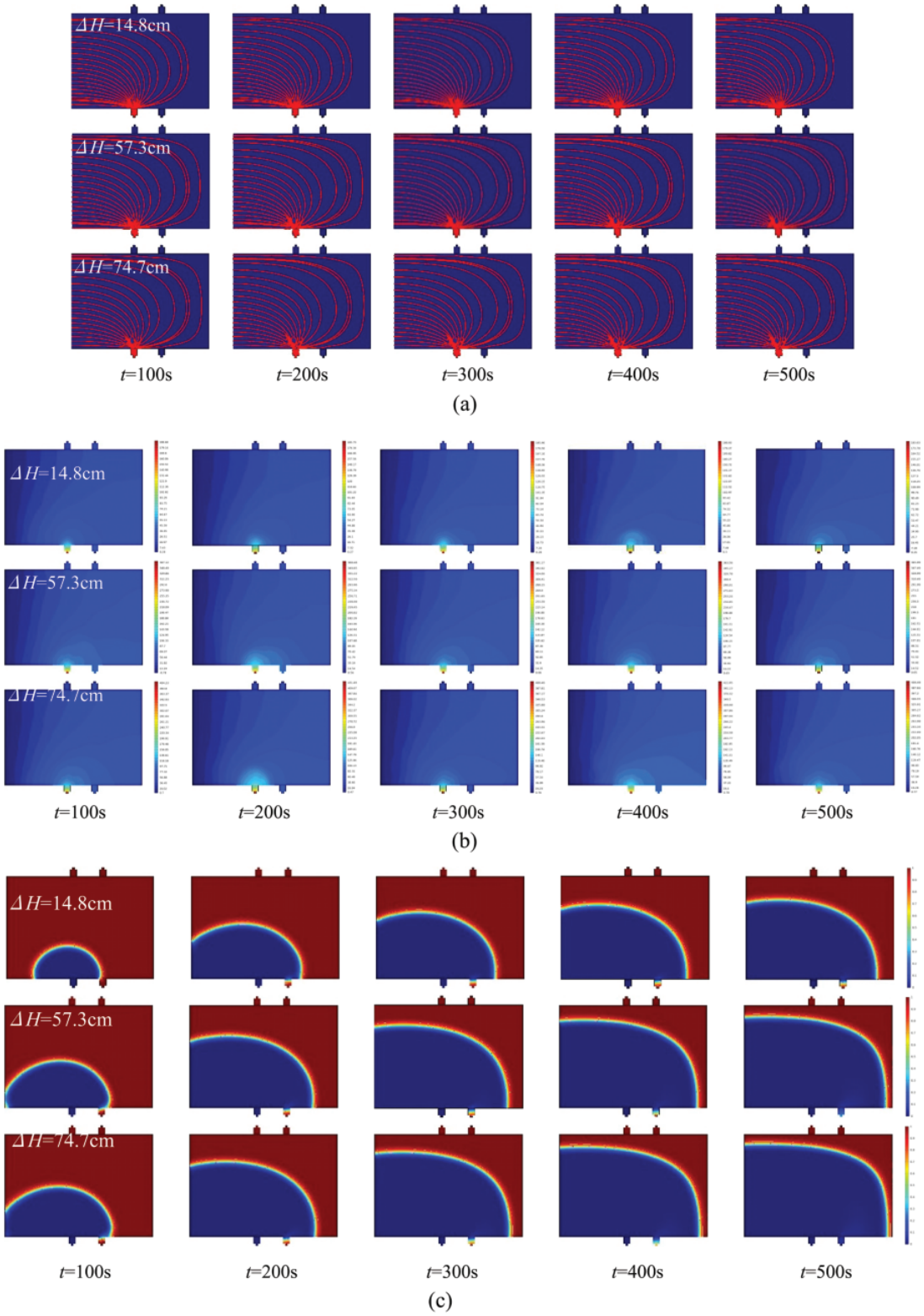

Figure 18: Effects of hydraulic heads on (a) flow streamlines, (b) hydraulic pressure fields, and (c) Numerical solute removal processes of the fracture surface with one inlet 3

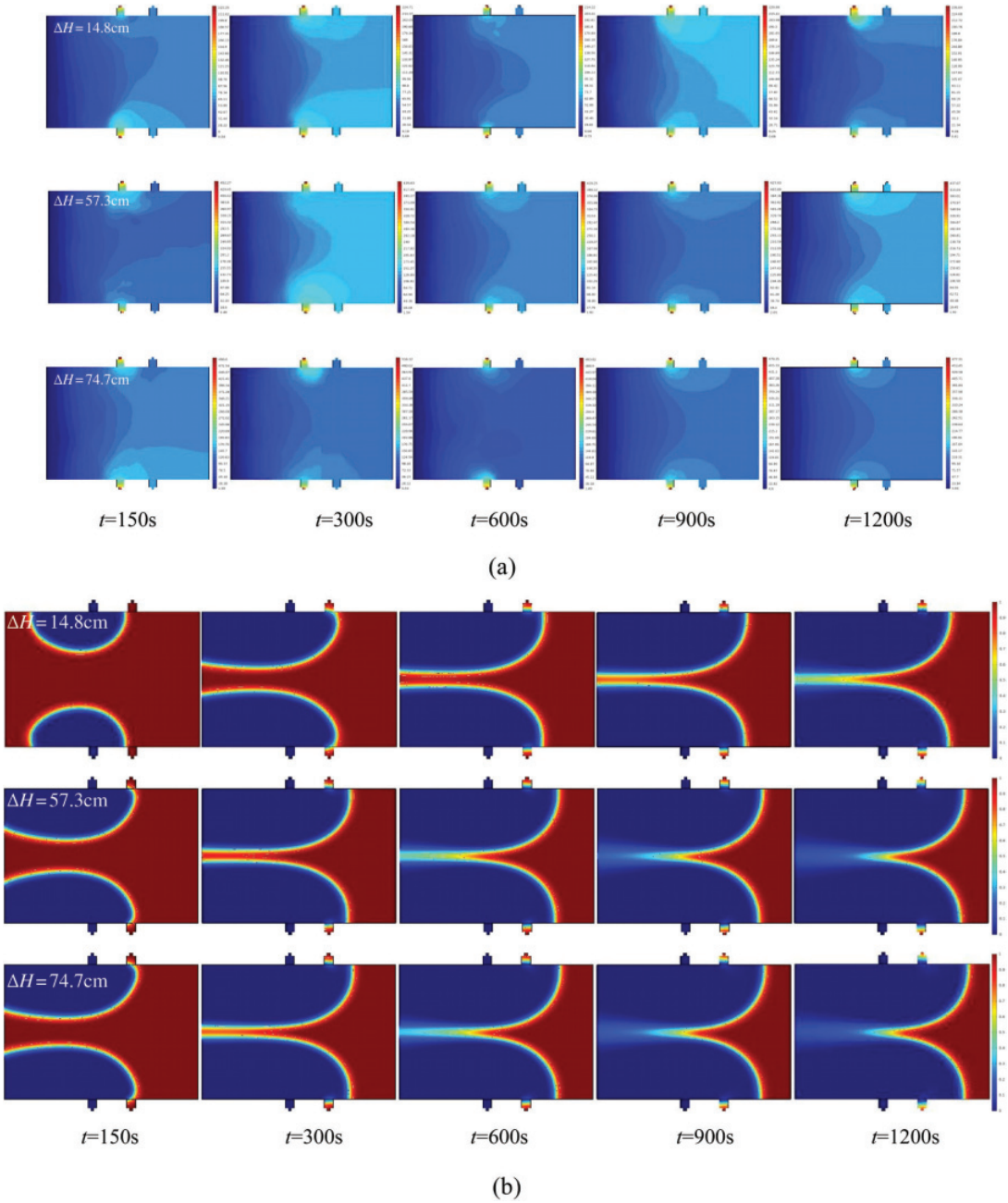

Figure 19: Effects of hydraulic heads on (a) flow velocity and flow streamlines, and (b) Numerical solute removal processes of the fracture surface with inlets 1 and 3

pressure fields, but both flow velocity and hydraulic pressure values increase with increasing ΔH. For the case of inlet 3 (Fig. 18), at a certain t, with an increase in ΔH, the distribution range of flow streamlines enlarges, and the maximum P value has more than doubled. For the case of inlets 1 and 3 shown in Fig. 19, due to the dominant role of inlet 1, the fracture planes are always filled with horizontal flow streamlines, while the maximum P value increases by a factor of 6. For a given ΔH, with increasing t, both the flow velocity fields and hydraulic pressure fields gradually develop to stable states. It should be noted that, both ΔH and t have dramatic influences on the solute removal processes. With continuous

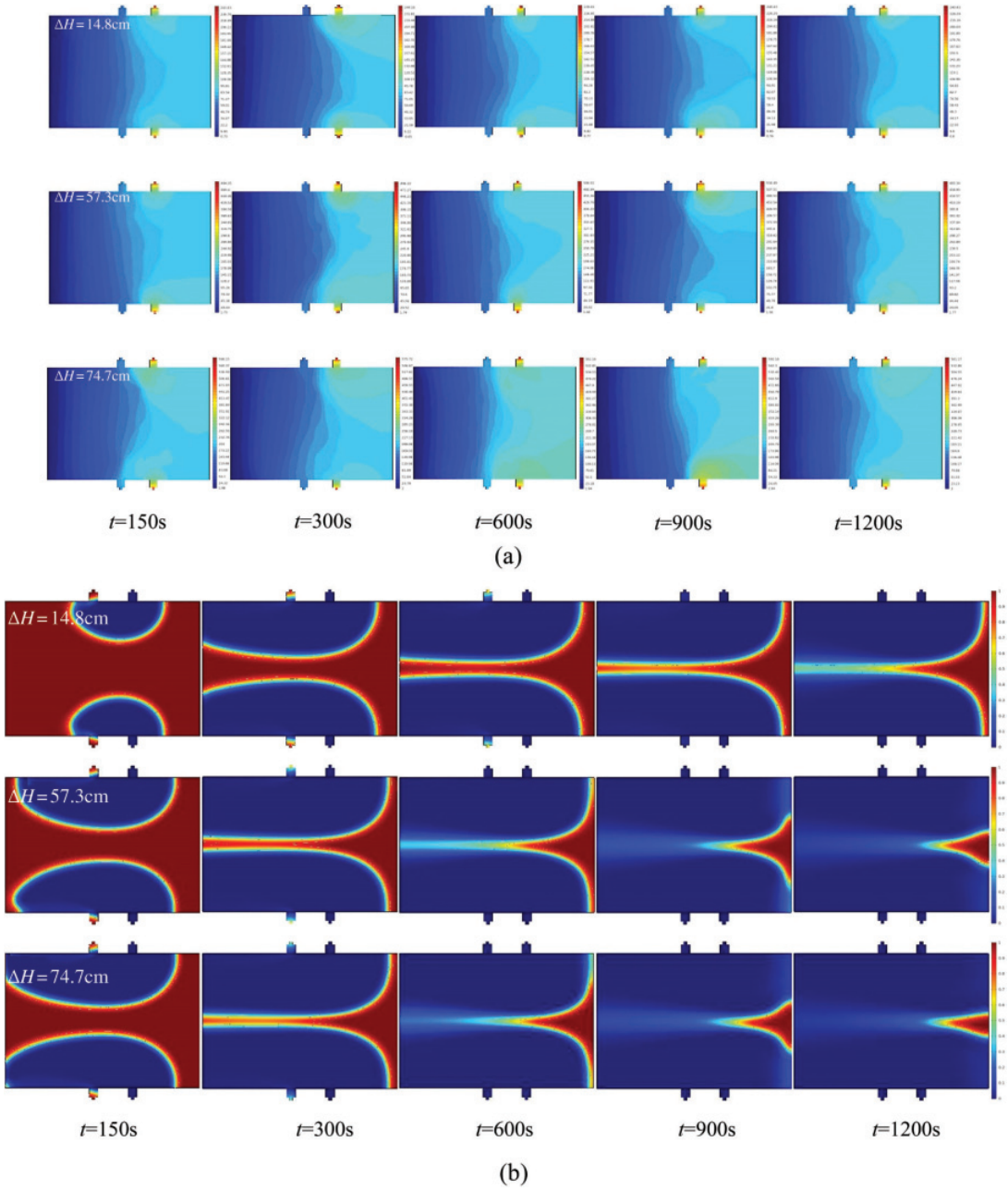

Figure 20: Effects of hydraulic heads on (a) hydraulic pressure fields, and (b) Numerical solute removal processes of the fracture surface with inlets 2 and 4

applied hydraulic pressure, the solute is gradually driven to the outlet, and the larger the ΔH value, the larger the concentration reduction rate of the solute. Interestingly, the "dead-ends" can be observed on the fracture surfaces, and moves in respect to various inlet combinations, located in the upper right corners of inlet 3, inlets 2 and 5, and middle right centers of inlets 2 and 4 and inlets 3 and 5.

Due to different solute removal processes of the fracture planes with various inlet combinations, the variations in dimensionless concentration also present a difference, as shown in Fig. 23. With an increase in t, the dimensionless concentration all declines from 1.0 at t = 0 s, and the rate of its decrease steadily

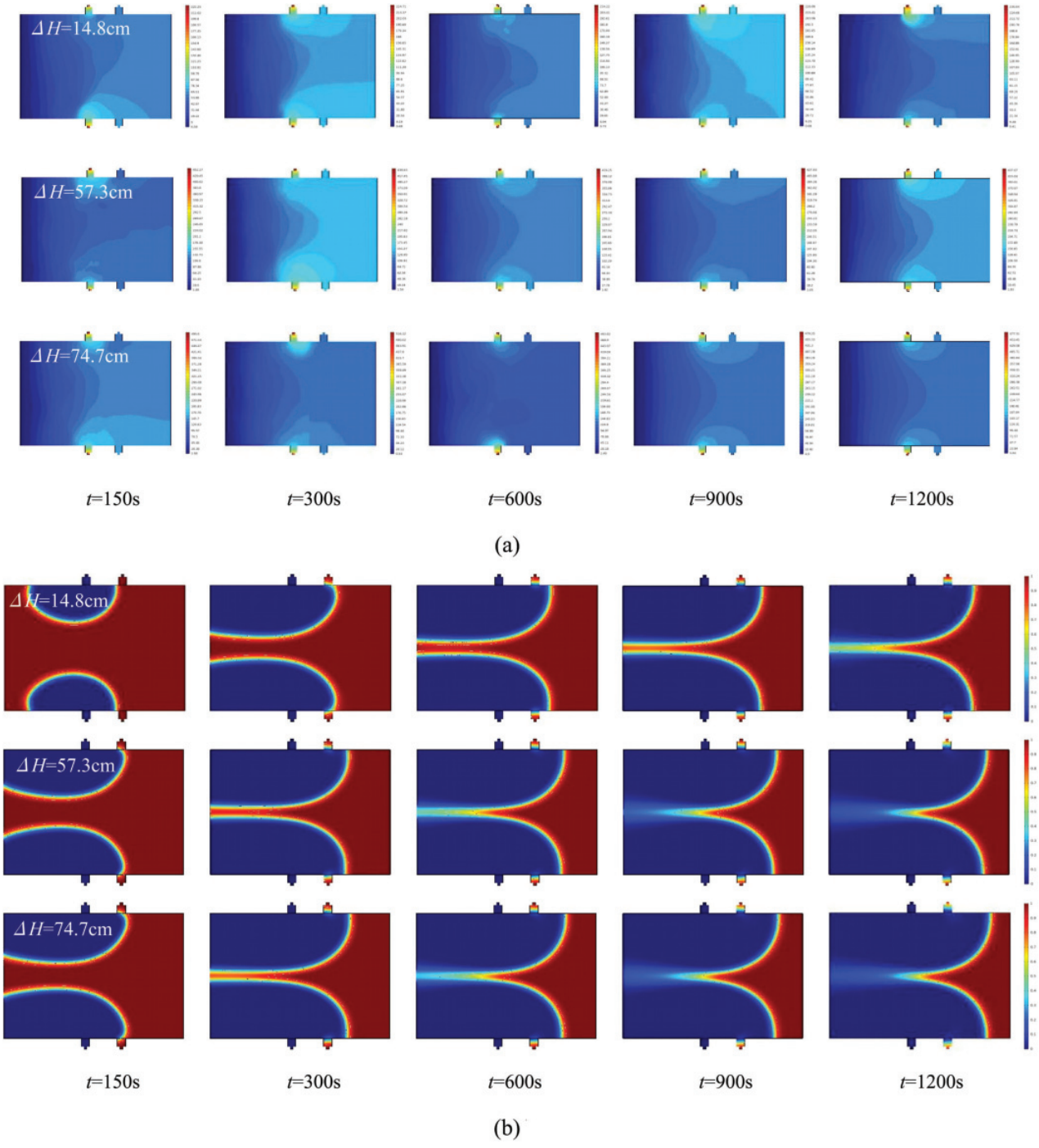

Figure 21: Effects of hydraulic heads on (a) hydraulic pressure fields, and (b) Numerical solute removal processes of the fracture surface with inlets 3 and 5

diminishes. Additionally, the variation curves shift downwards with an increase in ΔH, which indicates that the solute is driven faster to get into a steady state at a high hydraulic head difference. The cases of inlet 1, inlets 1 and 2, and inlets 1 and 3 present a larger attenuation speed, and the concentration finally declines to zero due to the dominant flow area and flow capacity of inlet 1. However, for the cases of inlet 2, inlet 3, inlets

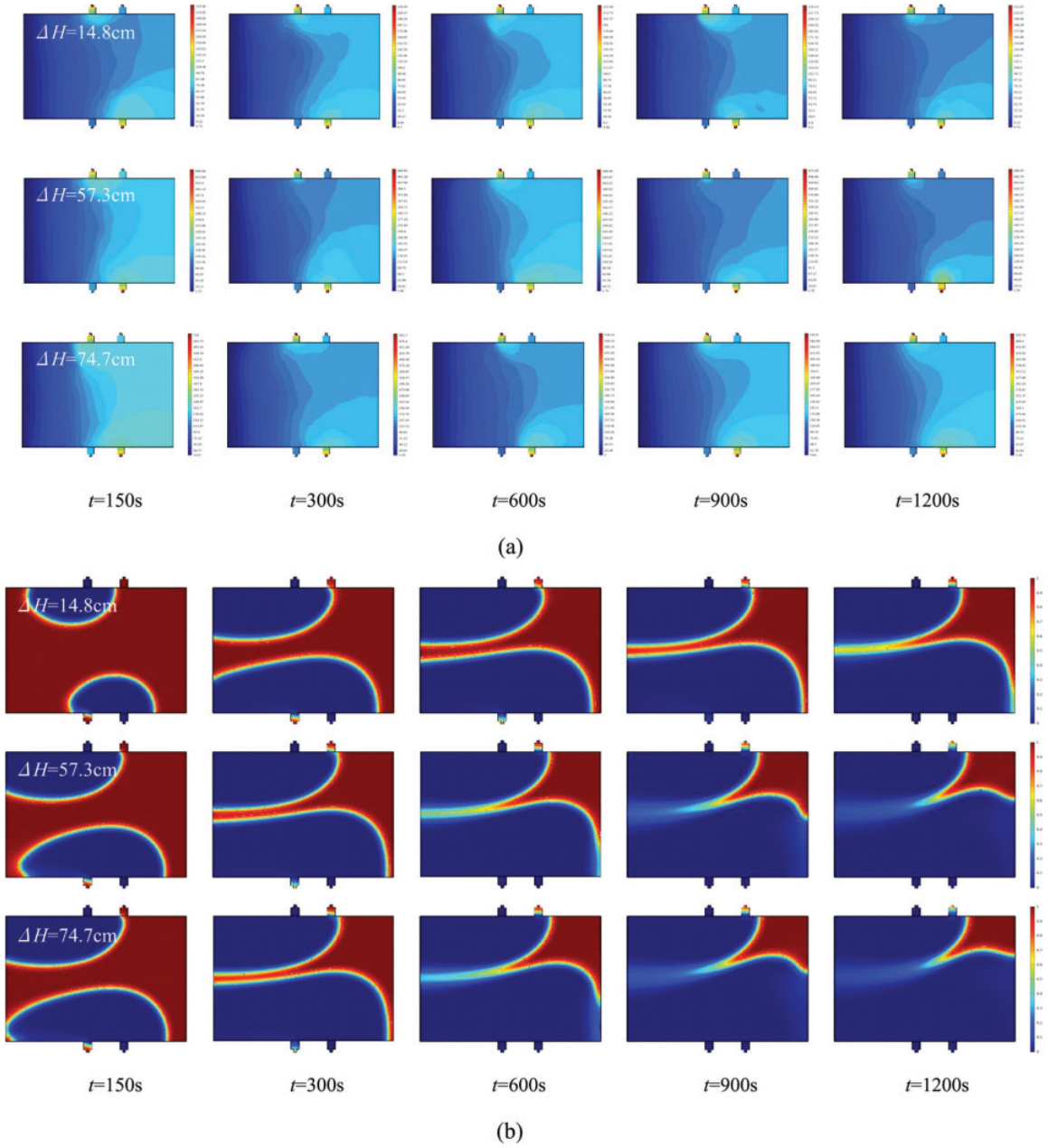

Figure 22: Effects of hydraulic heads on (a) hydraulic pressure fields, and (b) Numerical solute removal processes of the fracture surface with inlets 2 and 5

2 and 4, inlets 2 and 5, and inlets 3 and 5, the variation process of the dimensionless concentration can be divided into two stages, which first significantly varies, and then approaches constant values. Besides, due to the existing "dead-ends" of the fracture planes, the concentration cannot decline to zero, especially for the case of inlets 3 and 5.

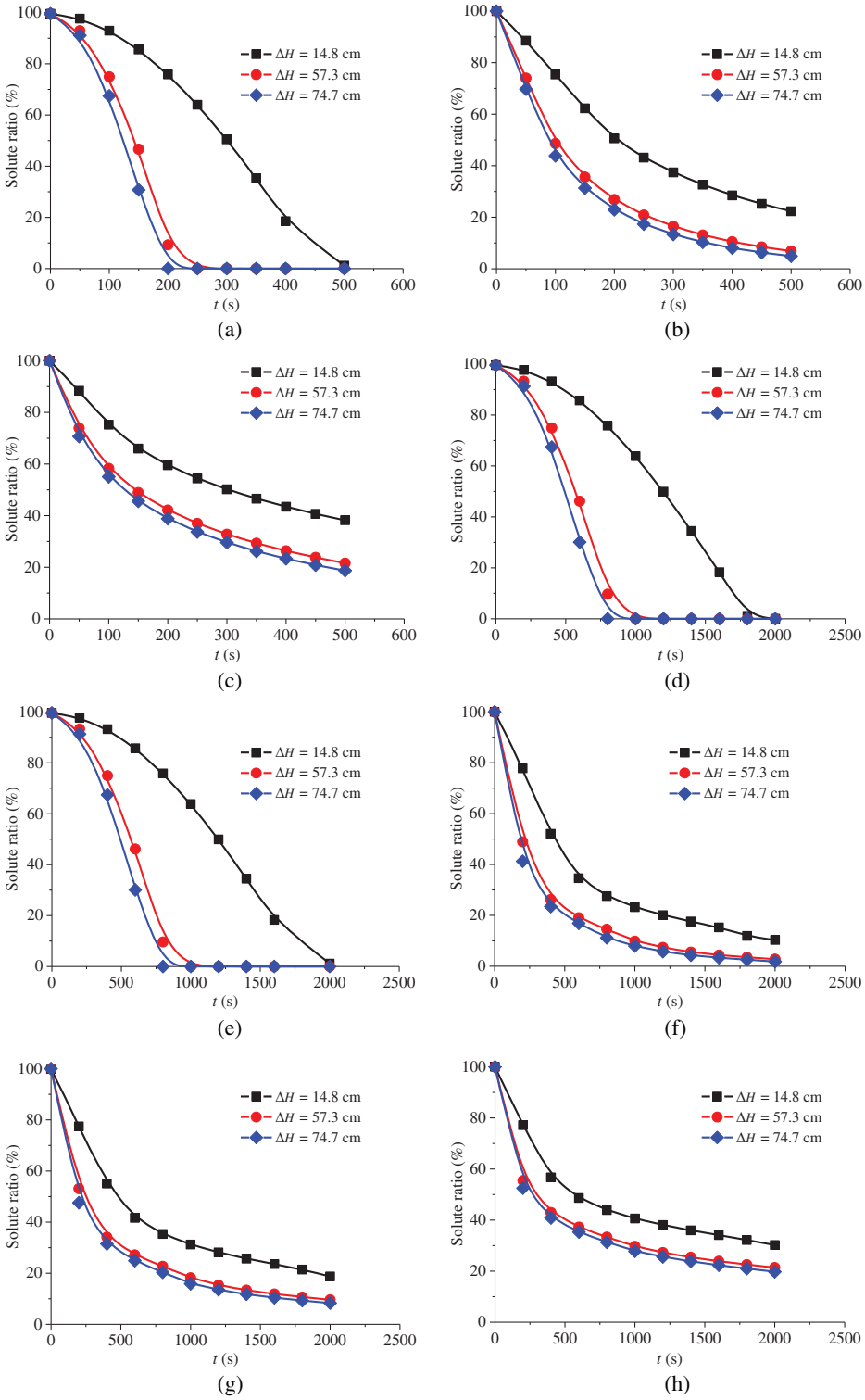

Figure 23: Numerically simulated variations in dimensionless concentration over time. (a) inlet 1, (b) inlet 2, (c) inlet 3, (d) inlets 1 and 2, (e) inlets 1 and 3, (f) inlets 2 and 4, (g) inlets 2 and 5, and (h) inlets 3 and 5

5 Conclusions

In this study, the solute removal process through large-scale fracture planes was experimentally investigated using a visualization technique, and then numerically simulated with the finite element software COMSOL multiphysics. Variations in the solute distributions, flow streamlines, hydraulic pressure fields and dimensionless concentration over time with respect to different flow paths and hydraulic head differences were analyzed.

(1) In the experiment, with the increment of time, the solute is removed significantly. Thus, the dimensionless concentration over time decreases from approximately 1, which is smaller than 1 due to the existence of bubbles. For the case of inlet 1, the velocity of fluid flow should theoretically be the same in the vertical direction, while there are some parts that fluid flows faster than other parts. This is induced by the rough fracture surface, which varies the aperture distribution along the vertical direction and then changes the fluid flow velocity. For the case of inlet 3, the interface between solute and water first shows a parabalo shape for a long time, which again illustrates that the water cannot flow through the "dead-ends", and the solute can only be removed by diffusion.

(2) The hydraulic head difference can decrease the time for solute removal, but the solute distribution changes sufficiently small. The flow path can significantly change the removal ability for solute. For the case of two inlets and one outlet, the solute will be robustly removed at the beginning when the pure water is injected into the inlet that is close to the outlet. With increasing time, the water cannot enter the "dead-ends" and remove the solute. However, the solute in the "dead-ends" can be effectively removed by injecting water into the inlet that is the longest to the outlet, which results in a short time that is needed to completely remove the solute in the fractures.

(3) Numerical simulations using the COMSOL multiphysics agree well with the experimental results regarding the variations in solute removal process and dimensionless concentration. For the cases of inlet 1, inlets 1 and 2 and inlets 1 and 3, due to the dominant flow capacity of inlet 1, the hydraulic pressure shows a uniform attenuation variation along the flowing path, with generally parallel flow streamlines. The solute concentration declines to zero at steady states. However, for the cases of inlet 2, inlet 3, inlets 2 and 4, inlets 2 and 5 and inlets 3 and 5, the flow streamlines are relatively complicated with obvious "dead-ends", thus the solute concentration cannot decrease to zero with increasing time.

(4) In practical engineering, the distance between the inlet and outlet boundaries of a fracture plane should be the longest, which can improve the solute removal ability. If the distance between the inlet and outlet boundaries of a fracture plane is not the longest, or even very close, the solute removal should be performed immediately, especially before the solute diffuses to the "dead-ends" of a fracture. This is because after the solute enters the "dead-ends" area, the solute is very difficult to be removed by advection, and can only be removed by diffusion, which is a time-consuming work. Additionally, it would be also interesting to bring insight to linkage between bubbles size and the created quantitative measures, and we will focus on this topic and conduct some related works in the future.

Acknowledgement: Financially support by National Natural Science Foundation of China, the Natural Science Foundation of Jiangsu Province, China, and State Key Laboratory for Geomechanics and Deep Underground Engineering, China University of Mining & Technology, China are appreciated.

Funding Statement: This work is financially supported by National Natural Science Foundation of China (Nos. 51979272, 51904290, 51979156), the Natural Science Foundation of Jiangsu Province, China (No. BK20180663), and State Key Laboratory for Geomechanics and Deep Underground Engineering, China University of Mining & Technology, China (No. SKLGDUEK1906).

Conflicts of Interest: The authors declare that they have no conflicts of interest to report regarding the present study.

References

1. Neretnieks, I. (1980). Diffusion in the rock matrix: an important factor in radionuclide retardation? *Journal of Geophysical Research: Solid Earth, 85(B8),* 4379–4397. DOI 10.1029/JB085iB08p04379.
2. Tang, D. H., Frind, E. O., Sudicky, E. A. (1981). Contaminant transport in fractured porous media: analytical solution for a single fracture. *Water Resources Research, 17(3),* 555–564. DOI 10.1029/WR017i003p00555.
3. Bodin, J., Delay, F., De Marsily, G. (2003). Solute transport in a single fracture with negligible matrix permeability: 1. fundamental mechanisms. *Hydrogeology Journal, 11(4),* 418–433. DOI 10.1007/s10040-003-0268-2.
4. Dou, Z., Zhou, Z. (2014). Lattice Boltzmann simulation of solute transport in a single rough fracture. *Water Science and Engineering, 7(3),* 277–287.
5. Fiori, A., Becker, M. W. (2015). Power law breakthrough curve tailing in a fracture: the role of advection. *Journal of Hydrology, 525,* 706–710. DOI 10.1016/j.jhydrol.2015.04.029.
6. Guihéneuf, N., Bour, O., Boisson, A., Le Borgne, T., Becker, M. et al. (2017). Insights about transport mechanisms and fracture flow channeling from multi-scale observations of tracer dispersion in shallow fractured crystalline rock. *Journal of Contaminant Hydrology, 206,* 18–33. DOI 10.1016/j.jconhyd.2017.09.003.
7. Zou, L., Jing, L., Cvetkovic, V. (2017a). Modeling of flow and mixing in 3D rough-walled rock fracture intersections. *Advances in Water Resources, 107,* 1–9. DOI 10.1016/j.advwatres.2017.06.003.
8. Zou, L., Jing, L., Cvetkovic, V. (2017b). Modeling of solute transport in a 3D rough-walled fracture-matrix system. *Transport in Porous Media, 116(3),* 1005–1029. DOI 10.1007/s11242-016-0810-z.
9. Dou, Z., Chen, Z., Zhou, Z., Wang, J., Huang, Y. (2018). Influence of eddies on conservative solute transport through a 2D single self-affine fracture. *International Journal of Heat and Mass Transfer, 121,* 597–606. DOI 10.1016/j.ijheatmasstransfer.2018.01.037.
10. Wang, G., Wang, K., Wang, S., Elswroth, D., Jiang, Y. (2018). An improved permeability evolution model and its application in fractured sorbing media. *Journal of Natural Gas Science and Engineering, 56,* 222–232. DOI 10.1016/j.jngse.2018.05.038.
11. Farlin, J., Gallé, T., Pittois, D., Bayerle, M., Schaul, T. (2019). Groundwater quality monitoring network design and optimisation based on measured contaminant concentration and taking solute transit time into account. *Journal of Hydrology, 573,* 516–523. DOI 10.1016/j.jhydrol.2019.01.067.
12. Huang, N., Jiang, Y., Liu, R., Li, B., Sugimoto, S. (2019a). A novel three-dimensional discrete fracture network model for investigating the role of aperture heterogeneity on fluid flow through fractured rock masses. *International Journal of Rock Mechanics & Mining Sciences, 116,* 25–37. DOI 10.1016/j.ijrmms.2019.03.014.
13. Huang, N., Liu, R., Jiang, Y., Cheng, Y., Li, B. (2019b). Shear-flow coupling characteristics of a three-dimensional discrete fracture network-fault model considering stress-induced aperture variations. *Journal of Hydrology, 571,* 416–424. DOI 10.1016/j.jhydrol.2019.01.068.
14. Grisak, G. E., Pickens, J. F. (1980). Solute transport through fractured media: 1. The effect of matrix diffusion. *Water Resources Research, 16(4),* 719–730. DOI 10.1029/WR016i004p00719.
15. Hull, L. C., Miller, J. D., Clemo, T. M. (1987). Laboratory and simulation studies of solute transport in fracture networks. *Water Resources Research, 23(8),* 1505–1513. DOI 10.1029/WR023i008p01505.
16. Haldeman, W. R., Chuang, Y., Rasmussen, T. C., Evans, D. D. (1991). Laboratory analysis of fluid flow and solute transport through a fracture embedded in porous tuff. *Water Resources Research, 27(1),* 53–65. DOI 10.1029/90WR01902.
17. Kennedy, C. A., Lennox, W. C. (1995). A control volume model of solute transport in a single fracture. *Water Resources Research, 31(2),* 313–322. DOI 10.1029/94WR01967.
18. Chen, F., Liu, X., Falta, R. W., Murdoch, L. (2010). Experimental demonstration of contaminant removal from fractured rock by boiling. *Environmental Science & Technology, 44(16),* 6437–6442. DOI 10.1021/es1015923.

19. Qian, J. Z., Chen, Z., Zhan, H. B., Luo, S. H. (2011). Solute transport in a filled single fracture under non-Darcian flow. *International Journal of Rock Mechanics & Mining Sciences, 48(1),* 132–140. DOI 10.1016/j.ijrmms.2010.09.009.
20. Sund, N. L., Bolster, D., Dawson, C. (2015). Upscaling transport of a reacting solute through a peridocially converging-diverging channel at pre-asymptotic times. *Journal of Contaminant Hydrology, 182,* 1–15. DOI 10.1016/j.jconhyd.2015.08.003.
21. Zhu, Y., Zhan, H., Jin, M. (2016). Analytical solutions of solute transport in a fracture-matrix system with different reaction rates for fracture and matrix. *Journal of Hydrology, 539,* 447–456. DOI 10.1016/j.jhydrol.2016.05.056.
22. Liu, L., Neretnieks, I., Shahkarami, P., Meng, S., Moreno, L. (2018). Solute transport along a single fracture in a porous rock: a simple analytical solution and its extension for modeling velocity dispersion. *Hydrogeology Journal, 26(1),* 297–320. DOI 10.1007/s10040-017-1627-8.
23. Delay, F., Badri, H., Ackerer, P. (2019). Heterogeneous hydraulic conductivity and porosity fields reconstruction through steady-state flow and transient solute transport data using the continuous adjoint state. *Advances in Water Resources, 127,* 148–166. DOI 10.1016/j.advwatres.2019.03.014.
24. Lucas, M., Cantareira, G. D., Wendland, E. (2019). Solute transport performance analysis of equivalent apertures in a single undisturbed basaltic fracture. *Hydrogeology Journal, 27(6),* 1999–2010. DOI 10.1007/s10040-019-01960-x.
25. Stanko, Z. P., Yeh, W. W. G. (2019). Nonlinear model reduction of solute transport models. *Advances in Water Resources, 130,* 157–171. DOI 10.1016/j.advwatres.2019.05.028.
26. Li, B., Liu, R., Jiang, Y. (2016). Influences of hydraulic gradient, surface roughness, intersecting angle, and scale effect on nonlinear flow behavior at single fracture intersections. *Journal of Hydrology, 538,* 440–453. DOI 10.1016/j.jhydrol.2016.04.053.
27. Liu, R., Jiang, Y., Li, B. (2016a). Effects of intersection and dead-end of fractures on nonlinear flow and particle transport in rock fracture networks. *Geosciences Journal, 20(3),* 415–426. DOI 10.1007/s12303-015-0057-7.
28. Liu, R. C., Li, B., Jiang, Y. J. (2016b). Critical hydraulic gradient for nonlinear flow through rock fracture networks: the roles of aperture, surface roughness, and number of interactions. *Advances in Water Resources, 88,* 53–65. DOI 10.1016/j.advwatres.2015.12.002.
29. Yin, Q., Ma, G. W., Jing, H. W., Wang, H. D., Su, H. J. et al. (2017). Hydraulic properties of 3D rough-walled fractures during shearing: an experimental study. *Journal of Hydrology, 555,* 169–184. DOI 10.1016/j.jhydrol.2017.10.019.
30. Yin, Q., Jing, H. W., Ma, G. W., Su, H. J., Liu, R. C. (2018). Investigating the roles of included angle and loading condition on the critical hydraulic gradient of real rock fracture networks. *Rock Mechanics and Rock Engineering, 51(10),* 3167–3177. DOI 10.1007/s00603-018-1526-x.
31. Wang, L., Cardenas, M. B., Slottke, D. T., Ketcham, R. A., Sharp, J. M. (2015). Modification of the Local Cubic Law of fracture flow for weak inertia, tortuosity, and roughness. *Water Resources Research, 51(4),* 2064–2080. DOI 10.1002/2014WR015815.
32. Yin, Q., Liu, R. C., Jing, H. W., Su, H. J., Yu, L. Y. et al. (2019). Experimental study of nonlinear flow behaviors through fractured rock samples after high-temperature exposure. *Rock Mechanics and Rock Engineering, 52(9),* 2963–2983. DOI 10.1007/s00603-019-1741-0.
33. Xie, L. Z., Gao, C., Ren, L., Li, C. B. (2015). Numerical investigation of geometrical and hydraulic properties in a single rock fracture during shear displacement with the Navier-Stokes equations. *Environmental Earth Sciences, 73(11),* 7061–7074. DOI 10.1007/s12665-015-4256-3.
34. Zou, L., Jing, L., Cvetkovic, V. (2015). Roughness decomposition and dynamic fluid flow in a single rock fracture. *International Journal of Rock Mechanics & Mining Sciences, 75,* 102. DOI 10.1016/j.ijrmms.2015.01.016.